The Astrophysical Journal, 964:53 (21pp), 2024 March 20 https://doi.org/10.3847/1538-4357/ad1ee3

Constrain the Dark-matter Distribution of Ultra-diffuse Galaxies with Globular-cluster Mass Segregation: A Case Study with NGC5846-UDG1

Jinning Liang[1,2], Fangzhou Jiang[1,3,4], Shany Danieli[5], Andrew Benson[3], and Phil Hopkins[4]
[1] Kavli Institute for Astronomy and Astrophysics, Peking University, Beijing 100871, People's Republic of China; fangzhou.jiang@pku.edu.cn
[2] School of Physics and Technology, Wuhan University, Wuhan, Hubei 430072, People's Republic of China
[3] Carnegie Observatories, 813 Santa Barbara Street, Pasadena, CA 91101, USA
[4] TAPIR, California Institute of Technology, Pasadena, CA 91125, USA
[5] Department of Astrophysical Sciences, 4 Ivy Lane, Princeton University, Princeton, NJ 08544, USA
Received 2023 May 8; revised 2023 December 9; accepted 2023 December 22; published 2024 March 14

Abstract

The properties of globular clusters (GCs) contain valuable information of their host galaxies and dark-matter halos. In the remarkable example of ultra-diffuse galaxy, NGC5846-UDG1, the GC population exhibits strong radial mass segregation, indicative of dynamical-friction-driven orbital decay, which opens the possibility of using imaging data alone to constrain the dark-matter content of the galaxy. To explore this possibility, we develop a semianalytical model of GC evolution, which starts from the initial mass, structural, and spatial distributions of the GC progenitors, and follows the effects of dynamical friction, tidal evolution, and two-body relaxation. Using Markov Chain Monte Carlo, we forward-model the GCs in a UDG1-like potential to match the observed GC statistics, and to constrain the profile of the host halo and the origin of the GCs. We find that, with the assumptions of zero mass segregation when the star clusters were born, UDG1 is relatively dark-matter-poor compared to what is expected from stellar-to-halo–mass relations, and its halo concentration is lower than the cosmological average, irrespective of having a cuspy or a cored profile. Its GC population has an initial spatial distribution more extended than the smooth stellar distribution. We discuss the results in the context of scaling laws of galaxy–halo connections, and warn against naively using the GC-abundance–halo–mass relation to infer the halo mass of ultra-diffuse galaxies. Our model is generally applicable to GC-rich dwarf galaxies, and is publicly available.

Unified Astronomy Thesaurus concepts: Galaxy dark matter halos (1880); Globular star clusters (656); Dynamical friction (422); Dwarf galaxies (416); Low surface brightness galaxies (940)

1. Introduction

Ultra-diffuse galaxies (UDGs) triggered a frenzy of studies in recent years in the contexts of both understanding the formation of extreme galaxies and testing cosmology (see, e.g., the review by Sales et al. 2020, and the references therein). Numerical and semianalytical simulations suggest that UDGs can form via supernovae-driven gas outflows, which transform their hosting dark-matter (DM) halos from cuspy to cored together with puffing up their stellar distribution (e.g., Di Cintio et al. 2017; Chan 2019; Jiang et al. 2019), while some UDGs can also populate halos of high specific angular momentum (e.g., Amorisco & Loeb 2016; Rong et al. 2017; Benavides et al. 2023). The formation of UDGs is also suggested to be facilitated in dense environments, via tidal heating (Carleton et al. 2019; Jiang et al. 2019; Liao et al. 2019) and passive stellar-population dimming (Tremmel et al. 2020). Despite all these theoretical efforts, there are still several aspects of UDGs that remain intriguing. Notably, UDGs on average have more globular clusters (GCs) than normal galaxies of similar stellar mass (van Dokkum et al. 2016, 2017; Lim et al. 2018; Forbes et al. 2020). There exists an empirical relation between GC abundance and DM halo mass, valid over almost 5 dex of virial mass for normal galaxies (Spitler & Forbes 2009; Hudson et al. 2014; Harris et al. 2015, 2017; Burkert & Forbes 2020). If this relation holds for UDGs, then a higher-than-average GC abundance implies that the host DM halo is overly massive for the stellar mass. In contrast, some UDGs seem to be DM deficient, based on their GC or gas kinematics (van Dokkum et al. 2018; Danieli et al. 2019; van Dokkum et al. 2019; Guo et al. 2020), which poses a challenge to the standard picture where galaxy formation takes place in DM halos that dominate the mass budget. Hence, to understand the GC populations of UDGs takes center stage in understanding UDG formation in a cosmological context. Notably, the abundance, the spatial distribution, and the kinematics of GCs all contain information of the DM distribution of their hosting UDG.

The galaxy NGC5846-UDG1 (UDG1 hereafter) serves as a remarkable example (Forbes et al. 2019, 2021; Müller et al. 2020; Danieli et al. 2022; Bar et al. 2022). On the one hand, it hosts a surprisingly large population of GCs (of $\sim$50 within two stellar effective radii) for its stellar mass of $\sim 10^8 M_\odot$. This translates to an overly massive DM halo of $\sim 10^{11} M_\odot$ assuming the Harris et al. (2017) relation (Forbes et al. 2021). On the other hand, the GC population of UDG1 shows a strong radial mass segregation (Bar et al. 2022), with more massive GCs lying closer to the center of the galaxy. The mass segregation can be most naturally interpreted as a manifestation of orbital decay caused by dynamical friction (DF), because the strength of DF scales strongly with the perturber mass. And if DF causes the mass segregation, the halo mass should be much lower, because the timescale of orbital decay depends on the perturber-to-host mass ratio (m/M), such that it is shorter than the dynamical timescale of the host galaxy only if $m/M \gtrsim 1/100$ (e.g., Boylan-Kolchin et al. 2008). That is, for a GC of

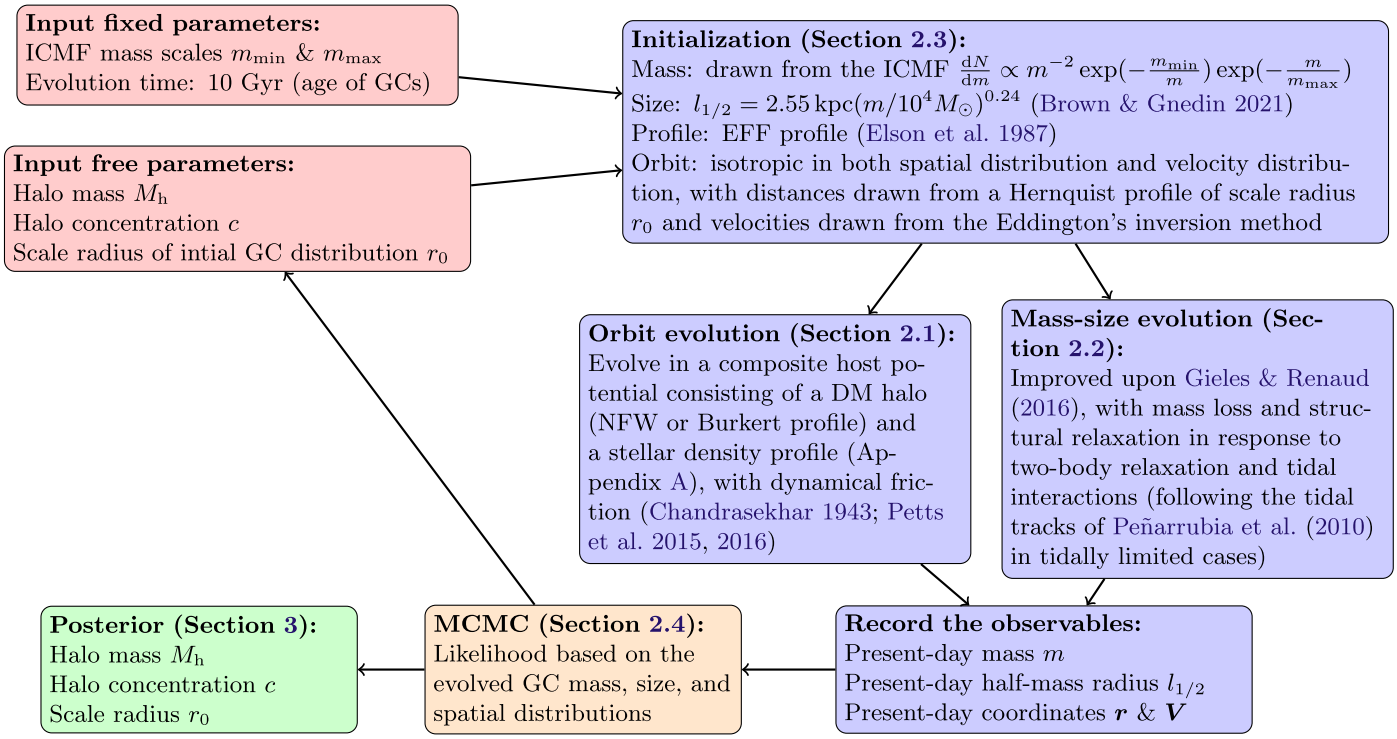

Figure 1. Model workflow. The `SatGen` (Jiang et al. 2021) semianalytical framework for galaxy evolution provides the backbone of this model. The star–cluster-specific prescriptions are summarized here and detailed in Section 2.

mass $m \sim 10^6 M_\odot$, the host halo cannot be orders of magnitudes more massive than the stellar component ($\sim 10^8 M_\odot$) in order to have sufficient orbital decay and mass segregation. Admittedly, this mass-ratio argument was originally made for satellite galaxies entering the host at orbital energies comparable to that of a circular orbit at the virial radius, so the GCs near the host center and thus with much lower orbital energy in principle allow for smaller mass ratios (and therefore larger host halo masses). This, however, requires more detailed modeling that considers the locations of the GCs at birth and the density profile of the host. The strikingly different halo–mass estimates based on the aforementioned two perspectives highlight the importance of such models.

In this work, we first present a semianalytical model of GC evolution in a composite host potential consisting of stellar and DM distributions. While generally applicable to any dwarf galaxy that exhibits a radial trend of its GC properties, here, this model is applied to UDG1 as a proof of concept, showing that the observed mass segregation, together with the other information of the GCs available in the imaging data, can be used to constrain the DM halo. As a major improvement over previous studies, which also attribute the GC mass segregation to DF (Bar et al. 2022; Modak et al. 2023), a more physical model of the evolution of star clusters under the influence of tidal interactions with the host galaxy and the internal two-body relaxation is considered. Tidal interactions and two-body relaxation drive mass loss and structural changes of the GCs, thus affecting the orbital evolution and the spatial distribution in a subtle but important way, as we will discuss below. When combined with parameter inference tools, this model enables using imaging data alone, without costly kinematics observations, to statistically constrain the DM distribution of the host galaxy. Additionally, the extreme limit of GC mass segregation is the complete orbital decay of massive GCs to the galaxy center, which is a viable way of forming dense nuclear star clusters (NSCs) as observed in nucleated low-surface-brightness galaxies (Greco et al. 2018; Lim et al. 2018; Sánchez-Janssen et al. 2019; Iodice et al. 2020; Marleau et al. 2021). Our method is therefore also potentially useful in this context.

This work is organized as follows. In Section 2, we introduce our model of GC evolution, and present the workflow of forward-modeling the GC population and inferring the host DM profile. For readers who wish to skip the technical details, Figure 1 presents a schematic flowchart that summarizes all the components of our framework, and serves as a self-contained starting place before reading the result sections. In Section 3, we use the observed GC statistics of UDG1 to constrain the model parameters, including the DM halo mass and concentration, as well as the characteristic spatial scale of the initial distribution of the GCs, which may shed light upon the origin of the GCs. In Section 4, we compare the model predictions and kinematics observations, discuss the key distinction between a cuspy halo profile versus a cored profile regarding star–cluster statistics, compare our model to simplistic models that ignore the physics of GC mass and structural evolution, and also comment on potential future developments of this methodology. We draw our conclusions in Section 5.

Throughout, we define the virial radius of the hosting DM halo as the radius within which the average density is $\Delta = 200$ times the critical density for closure, and adopt a flat cosmology with the present-day matter density $\Omega_{\rm m} = 0.3$, baryonic density $\Omega_{\rm b} = 0.0465$, dark energy density $\Omega_\Lambda = 0.7$, a power spectrum normalization $\sigma_8 = 0.8$, a power-law spectral index of $n_s = 1$, and a Hubble parameter of $h = 0.7$. We use r, R, and l to indicate the 3D galactocentric radius, the projected galactocentric radius, and star–cluster-centric radius, respectively; and denote the mass of a star cluster and that of the host galaxy by m and M, respectively.

2. Methodology

In this section, we first introduce a dynamical model that describes the evolution of GCs in a composite host potential consisting of DM and stars. This model considers the orbital evolution of GCs under the influence of DF, allowing for the dependence of the strength of DF on the local density profile of the host potential following the recipe of Petts et al. (2015). The GCs evolve in mass and structure in response to the internal two-body relaxation and the varying tidal effects along the orbits. We then lay out the model assumptions, including the initial star–cluster mass function, the initial structure of young star clusters, the initial spatial distribution of the star clusters, and the assumptions about the host potential. With these assumptions, the model self-consistently evolves a population of GCs, predicting their evolved masses, sizes, and spatial distribution, which are then compared to those of the observed GC population. Finally, we combine the model with a Markov Chain Monte Carlo (MCMC) inference tool, to derive constraints on the DM halo of the target galaxy. The workflow of our model is summarized in Figure 1. Our model is publicly available.[6]

2.1. Orbit Evolution

To follow the orbit of a GC, we solve the equation of motion,

$$\ddot{\boldsymbol{r}} = -\nabla\Phi + \boldsymbol{a}_{\rm DF}, \tag{1}$$

where $\boldsymbol{r}$ is the position vector, Φ is the gravitational potential, and $\boldsymbol{a}_{\rm DF}$ is the acceleration due to DF, given by Chandrasekhar (1943)

$$\boldsymbol{a}_{\rm DF} = -4\pi G^2 m \sum_i \ln\Lambda_i \rho_i(\boldsymbol{r}) F(<V_i) \frac{\boldsymbol{V}_i}{V_i^3}. \tag{2}$$

Here, the summation is over different components of the host potential (i = DM, stars), m is the mass of the GC, $\ln\Lambda_i$ is the Coulomb logarithm, $\boldsymbol{V}_i$ is the relative velocity of the GC with respect to component i, and $F(<V_i)$ is the fraction of particles that contribute to DF, which, under the assumption of a Maxwellian distribution, is given by $F(<V_i) = \mathrm{erf}(X_i) - (2X_i/\sqrt{\pi})e^{-X_i^2}$, where $X_i = V_i/(\sqrt{2}\sigma_i)$, with σ_i as the 1D velocity dispersion of component i at position $\boldsymbol{r}$.

In the idealized Chandrasekhar picture of DF, the perturber travels across an infinite homogeneous isotropic medium, and Λ is defined as $b_{\rm max}/b_{\rm min}$, with $b_{\rm max}$ and $b_{\rm min}$ as the maximum and minimum impact parameters, respectively. For the perturbers orbiting a galaxy, which is not a uniform medium, the Chandrasekhar DF treatment is used as an approximation, where $b_{\rm max}$ is of the order of the characteristic size of the host system, and $b_{\rm min}$ is the larger of the impact parameter for a 90° deflection and the size of the perturber (Binney & Tremaine 2008). In semianalytical models of satellite–galaxy evolution, it is a common practice to simply assume $\ln\Lambda \sim \ln(M/m)$, where M/m is the mass ratio of the host and the satellite, as the virial radius of a gravitationally bound structure scales with the virial mass (see, e.g., Gan et al. 2010, and the references therein). Even constant Coulomb logarithms of $\ln\Lambda \sim 3$ are widely adopted, as major and minor mergers ($M/m \lesssim 10$) contribute to the bulk of the surviving satellite galaxies. Hence, for the purpose of studying satellite galaxies, where typically the focus is not on the orbital evolution of individual perturbers but on the overall satellite statistics, the simplistic forms of Coulomb logarithm such as $\ln\Lambda \sim \ln(M/m)$ and $\sim$3 are reasonable (Green et al. 2021). However, for our purpose, here, i.e., to use the GC mass segregation to constrain the dynamical mass distribution, the details of individual orbits are important, and thus, the simplistic Coulomb logarithms for satellite galaxies may be problematic. For example, $\ln\Lambda \sim \ln(M/m)$ would be very high for GCs, and the orbital decay would be unrealistically strong.

Hence, following the more detailed treatment of Petts et al. (2015), we choose $b_{\rm max}$ to be

$$b_{\rm max}(r) = \min\left\{\frac{r}{\gamma(r)}, r\right\} \tag{3}$$

where $\gamma(r) \equiv -d\ln\rho/d\ln r$ is the local logarithmic density slope of the host potential, and choose $b_{\rm min}$ as

$$b_{\rm min} = \max\left\{l_{1/2}, \frac{Gm}{V^2}\right\}, \tag{4}$$

where $l_{1/2}$ is the half-mass–radius of the GC.[7] As such, $b_{\rm max}$ is a length scale over which the density is approximately constant (Just et al. 2011). To deal with the cases of $b_{\rm max} \sim b_{\rm min}$, which can happen when a GC approaches the center of the host, we use the original Chandrasekhar result for the Coulomb logarithm $0.5\ln(\Lambda^2+1)$ in place of the $\ln\Lambda$ in Equation (2). These choices empirically account for the core-stalling effect (Goerdt et al. 2006; Read et al. 2006; Inoue 2009; Kaur & Sridhar 2018), the phenomenon that the DF acceleration decreases, and the orbital decay stalls when the perturber approaches a flat density core—because in the density core, $\gamma(r) \sim 0$, $b_{\rm max} \sim b_{\rm min} \sim r$ and $\ln(\Lambda^2+1) \sim 0$.

Figure 2 compares the orbital evolution for different prescriptions of the Coulomb logarithm as well as for different GC mass evolution models, in a Navarro–Frenk–White (NFW) host halo and in a Burkert halo, respectively. Focusing on the comparison of the blue and black lines in either host profile, we can see that the simplistic Coulomb logarithm of $\ln(M/m)$ yields significantly stronger orbital decay than the more accurate Petts et al. (2015) treatment, which has been well calibrated against numerical simulations.

We also note that, in two previous studies that are highly relevant, Bar et al. (2022), Modak et al. (2023), the Coulomb logarithms were chosen to be simplified variants of what we use here. The key difference is that their models do not follow the size evolution of the GCs, so their $b_{\rm min}$ are effectively $\sim Gm/V^2$, which is usually a factor of a few smaller than $l_{1/2}$, making the Coulomb logarithm larger and DF stronger than the full treatment, in the NFW case as illustrated in the upper panel of Figure 2. In the Burkert case, Bar et al. (2022) model core stalling by setting Coulomb logarithm as zero when GCs get within 0.3 times the half-mass–radius of the galaxy. We will elaborate on the comparisons of our model with these models in Section 4.4.

[6] https://github.com/JiangFangzhou/GCevo

[7] In practice, we do not distinguish the half-mass–radius from the effective radius (i.e., 2D half-light radius), which is provided by the observational data for the GCs in UDG1 and the size–mass relation of young star clusters (Brown & Gnedin 2021, as will be discussed in Section 2.3).

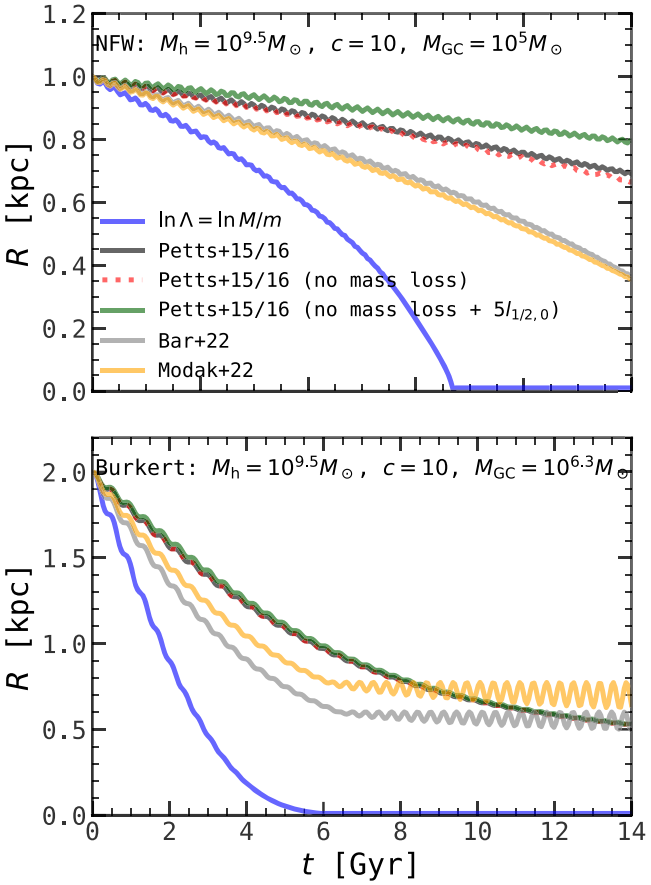

Figure 2. Illustration of the effects of different prescriptions of the Coulomb logarithm in the Chandrasekhar DF formula on the orbit evolution of a star cluster in a cuspy NFW host (upper) and in a cored Burkert host (lower), respectively. The parameters of the host halos and star clusters are chosen to better reveal the differences between different models, as indicated. The GCs are released at $t = 0$ on almost circular orbits. The black line stands for the result using our fiducial model of GC evolution (Section 2.2) and the Petts et al. (2015) Coulomb logarithm (Section 2.1). The other lines represent the results from varying certain aspect, using, e.g., the same fiducial Λ but with no mass loss (red), the same Λ but with no mass loss and with the GC size boosted by 5x (green), the fiducial evolution model but with a Λ widely assumed for satellite–galaxy evolution (blue). Note that, first, the GC mass–size evolution affects orbital evolution via the DF treatment; second, the Petts et al. (2015) Coulomb logarithm gives much weaker orbital decay than the simplistic $\ln\Lambda = \ln M/m$; third, the Bar et al. (2022) and Modak et al. (2023) recipes, which are simplified versions of Petts et al. (2015) that ignore the GC size in $b_{\min}$, result in stronger DF than the full treatment.

2.2. A Unified Model of Mass–Size Evolution

GCs are compact objects that are more resilient to the environmental processes than more diffuse substructures of a galaxy such as DM substructures and gas clouds. This is largely why, in several previous studies of GC mass segregation, the mass evolution of the GCs was treated simplistically, and the structural evolution of the GCs was completely ignored (Dutta Chowdhury et al. 2019; Bar et al. 2022; Modak et al. 2023). However, when dealing with the long-term evolution over the age of the clusters ($\sim$10 Gyr), the tidal interactions between the GCs and the host galaxy, especially near the center of the host, can result in nontrivial mass and structural change. In the meantime, GCs are internally collisional, and thus lose mass and expand due to the evaporation of stars. This is relevant even in low-density environments. The combination of the external tidal effects and the internal two-body relaxation may result in nonlinear mass loss and structural change, which, in turn, affects the orbital evolution, since the DF acceleration depends on the mass and structure of the perturber, as discussed in Section 2.1. Additionally, the imaging data of the GCs in nearby low-surface-brightness galaxies can be high-resolution enough to provide information about the internal structure of the GCs (van Dokkum et al. 2018). This potentially also contains valuable information of the dynamics besides the mere mass and spatial distribution. For all these reasons, we model the mass–size evolution of the GCs.

Our model of GC mass–size evolution adopts a similar formalism as that of Gieles & Renaud (2016, hereafter GR16) but is different in two important aspects. First, GR16 focused on the evolution of newly born star clusters younger than 100 Myr in the vicinity of their birth places, and therefore, the dominant tidal effect is the repeated impulsive encounters with giant molecular clouds in the clumpy interstellar medium surrounding the clusters. Here, we trace the long-term evolution of star clusters over cosmological timescales, and therefore, we focus more on the tidal interactions with the background potential. Second, because of the short-term nature, the GR16 model assumes that two-body relaxation causes no mass loss, whereas, here, we cannot ignore the mass loss from two-body relaxation over the age of the GCs. We assume that star clusters follow the (Elson et al. 1987, hereafter EFF) density profile with an outer density slope of -4, and the shape is fixed across evolution such that the density-profile evolution is manifested only by the mass and size evolution laid out below.

We start by differentiating the binding energy $E \propto -Gm^{5/3}\rho_{1/2}^{1/3}$ of a GC, and express the derivative in terms of the mass, m, and the average density within the half-mass–radius, $\rho_{1/2}$:

$$\frac{dE}{E} = \frac{5}{3}\frac{dm}{m} + \frac{1}{3}\frac{d\rho_{1/2}}{\rho_{1/2}}. \tag{5}$$

Both tidal interactions and two-body relaxation contribute to the energy increase dE and the mass-loss dm, so we distinguish their contributions by denoting dE and dm in two terms with subscripts "t" and "r," respectively,

$$\frac{dE_t + dE_r}{E} = \frac{5}{3}\frac{dm_t + dm_r}{m} + \frac{1}{3}\frac{d\rho_{1/2}}{\rho_{1/2}}. \tag{6}$$

Following GR16, we introduce a parameter f_t to relate the mass loss to the tidal heating from the interactions with the host potential:

$$\frac{dm_t}{m} = f_t\frac{dE_t}{E}. \tag{7}$$

Similarly, we define an f_r parameter that relates mass loss to the internal heating due to two-body relaxation:

$$\frac{dm_r}{m} = f_r\frac{dE_r}{E}. \tag{8}$$

The values of f_t and f_r can be estimated following analytical arguments or empirical numerical results, as will be elaborated shortly. It is easier to model the mass losses than to model the energy changes, so we proceed by eliminating the energy terms in Equation (6) using the definitions of f_t and f_r.

The mass loss from tidal stripping is computed as

$$\frac{dm_t}{m} = -\alpha\xi_t\frac{dt}{\tau_{\rm dyn}}, \tag{9}$$

where $\xi_t \equiv [m - m(l_t)]/m$ is the fraction of mass outside the tidal radius, with $m(l_t)$ as the mass within the instantaneous tidal radius, l_t; $\tau_{\rm dyn}$ is the dynamical time of the host potential at the GC's instantaneous location, given by

$$\tau_{\rm dyn} = \sqrt{\frac{3\pi}{16G\bar{\rho}(r)}}, \tag{10}$$

with $\bar{\rho}(r)$ as the average density of the host system within radius r; and $\alpha \approx 0.55$ is an empirical coefficient, calibrated with N-body simulations (Green et al. 2021). The tidal radius is given by King (1962)

$$l_t = r\left[\frac{m(l_t)/M(r)}{2 - d\ln M/d\ln r + V_t^2/V_{\rm circ}^2(r)}\right]^{1/3}, \tag{11}$$

where $M(r)$ is the host mass within radius r, $V_t = |\hat{r} \times \boldsymbol{V}|$ is the instantaneous tangential velocity, and $V_{\rm circ}(r)$ is the circular velocity.

Similarly, the evaporation caused by two-body relaxation can be expressed as

$$\frac{dm_r}{m} = -\xi_e\frac{dt}{\tau_r}, \tag{12}$$

where $\xi_e \equiv [m - m(< v_{\rm esc})]/m$ is the fraction of stars in the tail of the velocity distribution that is larger than the escape velocity, which, for an isolated relaxed GC and thus a Maxwellian velocity distribution, is a constant $\xi_e \approx 0.0074$; and τ_r is a relaxation timescale, given by Spitzer (1987), GR16

$$\tau_r \approx 0.142\ {\rm Gyr}\left(\frac{m}{10^4 M_\odot}\right)\left(\frac{\rho_{1/2}}{10^{11}M_\odot{\rm kpc}^{-3}}\right)^{-1/2}. \tag{13}$$

This is the timescale of refilling the high-speed tail of the velocity distribution.

Combining Equations (6)–(12), we obtain a unified model for GC structural evolution

$$\frac{d\rho_{1/2}}{\rho_{1/2}} = \left[\alpha\left(5 - \frac{3}{f_t}\right)\frac{\xi_t}{\tau_{\rm dyn}} + \left(5 - \frac{3}{f_r}\right)\frac{\xi_e}{\tau_r}\right]dt. \tag{14}$$

The parameters on the right-hand side of Equation (14) all have analytical estimates or empirical values based on numerical simulations.

GR16 adopted $f_t = 3$, and $f_r = 0$ for the short-term evolution of young star clusters in clumpy interstellar medium; here, we estimate f_t and f_r in the context of the long-term evolution of GCs in a gasless host. To estimate f_t, we consider the limit of negligible two-body relaxation, where the GC evolution can be approximated by the tidal evolution of self-gravitating collisionless systems, which has been extensively studied in the context of DM subhalos (e.g., Peñarrubia et al. 2010; Benson & Du 2022). Notably, Peñarrubia et al. (2010) calibrated the tidal evolutionary tracks for DM subhalos using N-body simulations in terms of the maximum-circular velocity $v_{\rm max}$ and the corresponding radius $l_{\rm max}$ as functions of the bound mass fraction $x = m(t)/m(0)$, and the inner logarithmic density slope $s = -d\ln\rho/d\ln l|_{l\to 0}$. Turning off two-body relaxation by setting the second term of Equation (14) to zero,

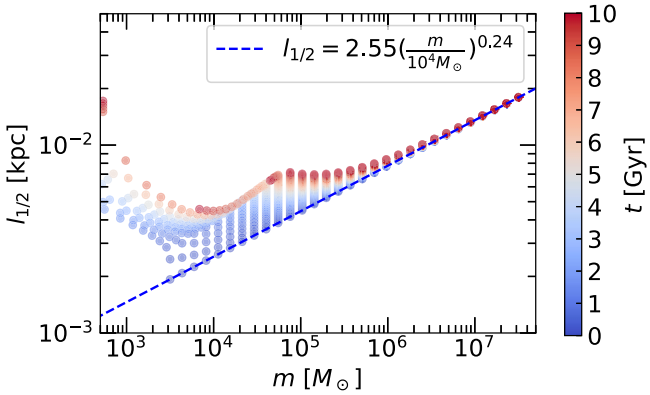

Figure 3. Illustration of the mass–size evolution of star clusters over 10 Gyr according to the model presented in Section 2.2. The star clusters are initialized with masses uniform in $\log m$, sizes following the observed size–mass relation of young star clusters (Brown & Gnedin 2021, blue dashed line), and circular orbits of $r = 5$ kpc in a host potential consisting of an NFW halo with $M_{\rm h} = 10^{12}M_\odot$, and $c = 10$ and a UDG1-like stellar profile. The evolution is mass-dependent, with massive clusters almost intact and low-mass clusters expanding first and then quickly getting tidally truncated and disrupted.

i.e.,

$$\frac{d\rho_{1/2}}{\rho_{1/2}} = \alpha\left(5 - \frac{3}{f_t}\right)\xi_t\frac{dt}{\tau_{\rm dyn}}, \tag{15}$$

we can therefore find f_t by matching the structural evolution according to Equation (15) in terms of $v_{\rm max}$ and $l_{\rm max}$ to the tidal track of Penarrubia et al. (2010) for the case of $s = 0$, since young star clusters are generally well described by the EFF profile and have flat density cores (see Section 2.3). We find that f_t is of the order of unity and mildly decreases with the bound mass fraction:

$$f_t = 0.77x^{0.19},\ x = m/m(0). \tag{16}$$

To estimate f_r, we follow Gieles et al. (2011) and the seminal work of Hénon (1965) to express the energy change of an isolated GC due to two-body relaxation as

$$\frac{dE_r}{E} = -\zeta\frac{dt}{\tau_r}, \tag{17}$$

where $\zeta \approx 0.0926$, assuming equal stellar masses of $0.5M_\odot$ and a Coulomb logarithm of 10 within the star cluster.[8] Comparing Equations (8), (12), and (17), we obtain

$$f_r = \xi_e/\zeta \approx 0.08. \tag{18}$$

In summary, for each timestep along the orbit, we evolve the mass of a GC using Equations (9) and (12), and update the structure of the GC using Equation (14), with the parameters $\alpha = 0.55$, $f_r = 0.08$, and f_t given by Equation (16). The initial mass and structure of a GC is chosen according to the assumptions that will be given in Section 2.3.

Figure 3 illustrates the behavior of GCs in the size–mass plane over 10 Gyr according to this model. The GCs are initialized with masses uniformly distributed in logarithmic mass and with sizes according to the median observed size–mass relation of young star clusters (Brown & Gnedin 2021, as will be discussed in Section 2.3). Clearly, the evolution depends on the initial mass. For the most massive GCs

[8] For any realistic stellar-mass spectrum, the ζ parameter is larger, up to $\sim$0.5 as discussed in GR16.

($m \gtrsim 10^6 M_\odot$), the size and mass barely evolve. For intermediately massive GCs ($m \approx 10^{5-6} M_\odot$), the main effect is expansion due to two-body relaxation, while the mass evolution is marginal. Basically, within 10 Gyr, the expansion barely makes their mass distribution extend to the tidal radius, so there is almost no tidal truncation. For lower-mass clusters ($m \lesssim 10^{4.5} M_\odot$), tidal truncation quickly takes effect as they expand, so they start to lose mass quickly and even dissolve. These mass-dependent behaviors work together to shape the evolved GC mass function in qualitatively the correct direction to that observed, peaking at $m \sim 10^5 M_\odot$. The evolved GC mass distribution would be insensitive to the low-mass end of the initial cluster mass function (ICMF). With low-mass GCs stripped and dissolved, intermediate-mass GCs experiencing weak DF, and massive GCs largely intact and thus always experiencing the strongest DF, mass segregation would naturally arise.

2.3. Model Assumptions and GC Initialization

We emphasize that the scenario that this study focuses on is that the observed GC mass-segregation signal is driven by DF and that the strength of it can be used to constrain the DM distribution of the host galaxy. Hence, the assumptions are chosen to keep the setup simple and to serve the purpose of testing the constraining power of GC mass segregation on DM halo properties. We assume that the ICMF follows a power law with exponential truncations at both the high-mass and low-mass ends (Trujillo-Gomez et al. 2019):

$$\frac{\mathrm{d}N}{\mathrm{d}m} \propto m^{\beta} \exp\left(-\frac{m_{\rm min}}{m}\right) \exp\left(-\frac{m}{m_{\rm max}}\right), \tag{19}$$

where $\beta = -2$ reflects hierarchical molecular cloud formation, and $m_{\rm min}$ and $m_{\rm max}$ are the lower and upper characteristic scales. We keep $m_{\rm min} = 10^{5.5} M_\odot$, and $m_{\rm max} = 10^8 M_\odot$ fixed for simplicity, after having verified that the results are not sensitive to the detailed values as long as they allow for the existence of GCs covering the mass range of $\sim 10^{4.5}$–$10^6 M_\odot$.[9] This is partly due to the mass-dependent evolution as shown in Figure 3, that the low-mass clusters will dissolve in the end.

We describe the density profile of a star cluster by an EFF functional form,

$$\rho(l) = \frac{\rho_0}{(1 + l^2/a^2)^{\eta}}, \tag{20}$$

where $\rho_0 = \Gamma(\eta) m / [\pi^{3/2} \Gamma(\eta - 1) a^3]$ is the central density, with $\Gamma(x)$ as the gamma function, m as the mass of the cluster, -2η as the outer logarithmic density slope, and a as a scale radius linked to the half-mass–radius by

$$a = l_{1/2} / (2^{\frac{2}{2\eta - 3}} - 1)^{1/2}. \tag{21}$$

We adopt $\eta = 2$ such that the outer density slope is -4, motivated by observations of the light profile of young star clusters (Ryon et al. 2015), and assume that the slope is fixed across the evolution such that the density-profile evolution is manifested only by the mass and size evolution as in Section 2.2. More analytical properties of the EFF profile are presented in Appendix B.

With the initial mass drawn from the ICMF, we determine the initial size by sampling from a log-normal distribution based on the observed size–mass relation for young star clusters in the Legacy Extragalactic UV Survey (Brown & Gnedin 2021): the median half-mass–radius is given by

$$l_{1/2} = 2.55 \text{ kpc} \left(\frac{m}{10^4 M_\odot}\right)^{0.24}, \tag{22}$$

and the 1σ scatter at fixed mass is approximately 0.25 dex.

We assume that the GC progenitors were all born 10 Gyr ago (Müller et al. 2020; Bar et al. 2022) and that they were isotropically distributed following a Hernquist (1990) profile, $\rho(r) \propto 1/[r(r + r_0)^3]$, with no mass segregation at birth. We briefly explore the possibility of an initial mass segregation in Appendix D. The initial spatial scale, r_0, of the GC-progenitor spatial distribution is a free parameter to be constrained. We note that the GC–GC merger rate is only $\sim 0.03\,\mathrm{Gyr}^{-1}$ per GC assuming ~ 100 GCs in a dwarf halo of $10^{10} M_\odot$, using the merger criterion in Dutta Chowdhury et al. (2020). We have also numerically verified, using the GC-merger prescription of Modak et al. (2023), that, for such a dwarf halo, GC mergers almost all occur at $r \lesssim 0.1$ kpc. Hence, to facilitate the MCMC inference, we practically ignore GC–GC encounters and mergers when focusing on the radial mass-segregation signal at $r > 0.1$ kpc. For the GCs that have lost most of their orbital angular momenta and settle to $r < 0.1$ kpc before getting dissolved, we treat them as merging to form an NSC (see Section 4.2).

We treat the host system as a combination of a smooth stellar-mass distribution and a DM halo, both of which remain static during the GC evolution. For the stellar profile, to facilitate orbit integration, we fit a density profile with simple analytical expressions of the gravitational potential to the observed stellar density profile (Bar et al. 2022), given by

$$\rho(r) = \frac{\rho_{0,\star}}{(1 + x)(1 + x^3)} \tag{23}$$

where $x = r/r_{\rm s}$, and $\rho_{0,\star} = 27 M_\star / [4\pi (9 + 2\sqrt{3}\pi) r_{\rm s}^3]$, with $M_\star = 10^{8.3} M_\odot$, and $r_{\rm s} = 2$ kpc (see Appendix A.3 for more details). For the DM halo, we consider representative functional forms for cuspy and cored profiles, respecitvely—namely, the NFW (Navarro et al. 1997) profile,

$$\rho(r) = \frac{\rho_0}{x(1 + x)^2}, \tag{24}$$

where $x = cr/r_{\rm vir}$, and $\rho_0 = c^3 \Delta \rho_{\rm crit} / [3 f(c)]$, with $f(x) = \ln(1 + x) - x/(1 + x)$; and the Burkert (1995) profile,

$$\rho(r) = \frac{\rho_0}{(1 + x)(1 + x^2)}, \tag{25}$$

where $x = cr/r_{\rm vir}$, and $\rho_0 = M_{\rm h} / [2\pi r_{\rm vir}^3 g(c) c^3]$, with $g(x) = 0.5 \ln(1 + x^2) + \ln(1 + x) - \arctan x$. It is not obvious whether a core or a cusp is more advantageous for producing the GC mass segregation: for a cored profile, GCs would pile up where the density slope turns flat due to the core-stalling effect, so that the massive GCs that sink to the core radius and the lower-mass GCs that were initially at the core radius are mixed; for a cuspy profile, DF could be so strong that massive GCs sink completely to the center, but leaving the outer GCs

[9] We emphasize that $m_{\rm min}$ should not be regarded as the minimum initial mass: because of the functional form of Equation (19) and the power-law slope of $\beta = -2$, with $m_{\rm min} = 10^{5.5} M_\odot$, the minimum initial star–cluster mass can reach $\sim 10^4 M_\odot$. Similarly, $m_{\rm max}$ is not the maximum GC mass.

not very different in mass. It is therefore interesting to explore which case produces mass segregation more easily and what other differences they may cause.

We initialize the velocities of the star clusters by sampling the velocity distribution function $\mathcal{P}(V|r)$ of a statistically steady-state system in absence of DF. Specifically, the ergodic energy distribution function is calculated from the Eddington's inversion method (Binney & Tremaine 2008),

$$f(\mathcal{E}) = \frac{1}{\sqrt{8}\,\pi^2}\left[\frac{1}{\sqrt{\mathcal{E}}}\left(\frac{d\rho}{d\Psi}\right)_{\Psi=0} + \int_0^{\mathcal{E}} \frac{d\Psi}{\sqrt{\mathcal{E}-\Psi}}\frac{d^2\rho}{d\Psi^2}\right], \quad (26)$$

where $\Psi(r) = -\Phi(r)$, with Φ and ρ as the gravitational potential and density profile of the DM halo. Then, the conditional distribution of velocities at each radius r is given by

$$\mathcal{P}(V|r) = 4\pi V^2 \frac{f(\Psi(r) - V^2/2)}{\rho(r)}. \quad (27)$$

We draw the speeds from $\mathcal{P}(V|r)$ and assign the directions of the velocity vectors such that they are isotropic in space (e.g., as detailed in Jiang et al. 2021).

2.4. Parameter Inference

We use the affine invariant MCMC ensemble sampler, `emcee` (Foreman-mackey et al. 2013), to constrain the properties of the host DM halo (i.e., the halo mass $M_{\rm h}$ and the halo concentration parameter c) and the initial scale length of the GC distribution r_0. The observational data that provide the constraints involves the present-day masses of the GCs (m), the half-mass radii ($l_{1/2}$), and the projected distances to the galaxy center (R), from Danieli et al. (2022).[10] With the primary focus being the radial segregation in mass, we adopt three logarithmic mass bins (as indicated in Figure 5), and use the median quantities $\langle \log m\rangle_i$, $\langle l_{1/2}\rangle_i$, and $\langle \log R\rangle_i$ for constructing the likelihood. We parameterize the radial mass segregation using two sets of quantities: the slopes $\gamma_{ij} \equiv (\langle \log m\rangle_j - \langle \log m\rangle_i)/(\langle \log R\rangle_j - \langle \log R\rangle_i)$, and the number of GCs at each bin relative to the total number of the surviving GCs, f_i. These two quantities measure the steepness of the radial mass segregation and sample the evolved GC mass function, respectively. Overall, we consider a logarithmic likelihood given by

$$\ln(p) = -\frac{1}{2}\sum_k w_k \frac{(y_{k,\rm data} - y_{k,\rm model})^2}{y_{k,\rm data}^2}, \quad (28)$$

where $y_{k,\rm data}$ and $y_{k,\rm model}$ refer to the observed values and model predictions, respectively, and y_k represents one of the following quantities, $\{\langle \log m\rangle_i\}$, $\{\langle \log R\rangle_i\}$ $\{\langle l_{1/2}\rangle_i\}$, $\{\langle\gamma\rangle_{ij}\}_{j>i}$, and $\{f_i\}$, with $i, j = 1, 2, 3$ the mass-bin indices, and w_k as the weight for the kth quantity. We adopt uniform weighting ($w_k = 1$), which essentially gives the mass-segregation signal an emphasis because there are three γ_{ij} slopes that measure it. We adopt uniform priors for $\log M_{\rm h}$, $\log c$, and the initial spatial scale r_0, within ranges that are chosen according to the galaxy of interest (see Section 3 for example).

To speed up the MCMC inference, instead of evolving the GC populations on the fly for each iteration, we precompute the model predictions $y_{k,\rm model}$ on a mesh grid spanned by the parameters of interest. During the MCMC random walk, $y_{k,\rm model}$ is evaluated by linear interpolation. Examples of the precomputed models can be seen in Appendix C. Note that we opt for not including the total number of GCs as a quantity of interest in our model. This allows us to focus more efficiently on the correlations and on the moments of the observables. Hence, when precomputing the models, we adopt arbitrarily large initial number of GCs to ensure smooth interpolations. Note that ignoring GC mergers is inevitable in this approach, since the merger rate depends on the total number. With that said, when presenting the model realizations corresponding to the posterior models, we adopt an initial GC number that leads to a surviving GC abundance comparable to what is observed.

3. The Dark-matter Halo of NGC5846-UDG1

As a proof of concept, we apply the aforementioned method to study the halo of UDG1 and its GC population. We assume uniform priors of $\log(M_{\rm h}/M_\odot) \in [8, 10.5]$, $\log c \in [\log 2, \log 30]$, and $r_0 \in [1, 5]$ kpc, and choose $M_{\rm min} = 10^{5.5} M_\odot$, and $M_{\rm max} = 10^8 M_\odot$ for the ICMF, and evolve GCs for 10 Gyr, after verifying that the results are not sensitive to slight variations of these values. We use 64 random walkers, and show results of 20,000 iterations after 1000 burn-in timesteps. Below, we first present the posterior distributions of the parameters, then compare model realizations with the best-fit parameters with the data, for the two halo–profile scenarios respectively, and finally discuss the results in the context of scaling relations of galaxy–halo connection.

3.1. NFW Halo

Figure 4 shows the posterior distributions for NFW host halos. The mode values (in the 3D parameter space) are $M_{\rm h} = 10^{9.1} M_\odot$, $c = 4$, and $r_0 = 3.1$ kpc, as indicated by the red stars. The median values, together with the 16th and 84th percentiles, are $\log(M_{\rm h}/M_\odot) = 8.9^{+0.7}_{-0.5}$, $c = 6.0^{+8.4}_{-3.1}$, and $r_0 = 3.2^{+1.2}_{-1.4}$ kpc, as indicated by the red lines. Figure 5 shows a model realization with the mode parameters, with 300 star clusters intially.

First, focusing on the R–m plane of Figure 5, there is a clear trend of mass segregation in the model realization, very similar to that observed. The parameter space that can give rise to such a prominent mass segregation is actually rather limited: a halo significantly more massive than $10^{9.5} M_\odot$ can hardly reproduce the slope and the small distances of the most massive GCs, irrespective of how c or r_0 is varied (see, e.g., Appendix C).

Second, the evolved GC size distribution and the size–mass relation are reproduced fairly well: note that the initial GC size distribution is quite broad, but the evolution shrinks the size distribution to better match that observed. Related, the evolved GC size–mass relation is almost flat, as observed, while the initial one has a slope of 0.24. These two trends are largely because the low-mass GCs expand due to two-body relaxation and tidal interactions while the massive ones are almost intact, as discussed in Figure 3.

[10] Note that the half-mass radii and masses were not published in their original work. We have used the full width at half-maximum (FWHM) sizes to estimate the half-mass radii, as $l_{1/2} = \mathrm{FWHM}/2$. We obtain the GC masses using $m = \gamma L_V$, where γ is the mass-to-light ratio, set to be 1.6 (Müller et al. 2020), and L_V is V-band luminosity. We only include the GC candidates with $M_V < 25$ mag, which gives us a sample of 34 GCs.

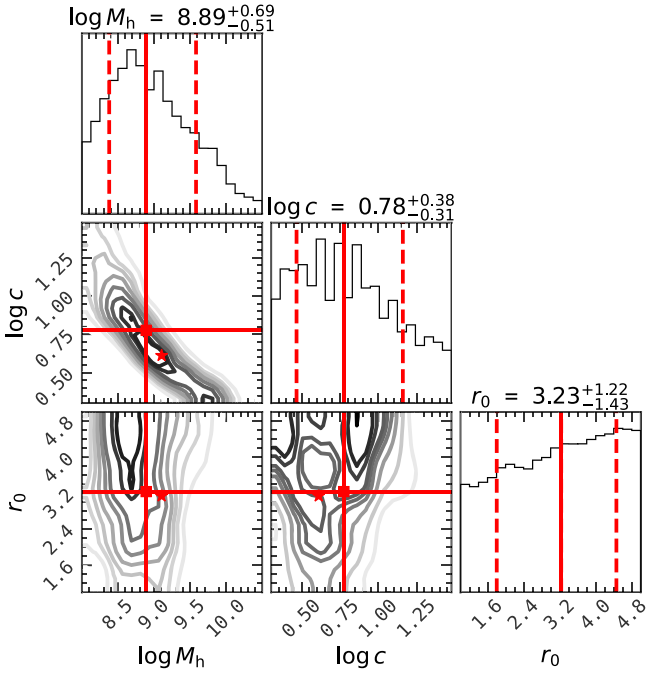

Figure 4. Posterior distributions of the model parameters (halo mass M_h, halo concentration c, and the scale radius r_0 for the initial star–cluster distribution), assuming an NFW host halo. The red lines indicate the median and the 16th and 84th percentiles. The red stars indicate the 2D projections of the 3D mode value.

Third, the GC mass distribution evolves from an initial broad one toward a narrower distribution in better agreement with what is observed. This is partly because of the depletion of the lowest-mass clusters ($m \lesssim 10^{4.5} M_\odot$), but also partly because some of the most massive clusters ($m \gtrsim 10^6 M_\odot$) have sunk to the center of the system to contribute to the formation of an NSC and thus are not taken into account here. We will discuss this further in Section 4.

As can be seen from the posteriors in Figure 4, there is an anticorrelation between halo concentration c and halo mass M_h. This degeneracy is driven by the mass segregation, which can only be achieved with an appropriate amount of DF— overly strong DF would result in orbital decay that is too fast, such that all the massive GCs sink to the center, forming a stellar nucleus instead of a continuous radial mass gradient; overly weak DF would have no effect. Ignoring the Coulomb logarithm, the strength of DF at a radius r can be estimated with the quantity $r\rho(r)/M(r)$, as can be seen from Equation (2), where the DF acceleration $a_{\rm DF}$ scales linearly with the local density $\rho(r)$ and inversely with the velocity squared, $V^2 \sim GM(r)/r$. For NFW profiles, it is easy to show that this quantity increases with increasing halo mass or concentration, for the radius range of interest ($r \lesssim 5$ kpc). This is not the case for a Burkert profile, as will be discussed shortly in Section 3.2.

At the posterior median value, the halo mass of $M_h \sim 10^9 M_\odot$ corresponds to a $M_\star/M_h$ ratio of ~0.1, much higher than that of normal galaxies. Also, interestingly, the concentration is much lower than the cosmological average values. The expected halo concentration is ~25 (Dutton & Macciò 2014) for a halo mass of $M_h \sim 10^9 M_\odot$, ~3σ higher than the posterior median. We discuss the implications of these findings in Section 3.3.

The initial star–cluster distribution, with a scale distance of $r_0 \sim 3$ kpc, is more extended than the present-day smooth stellar distribution of UDG1, which has an effective radius of 2 kpc. This may provide clues for understanding star cluster formation. One scenario is that the star clusters may have formed ex situ and been brought in by satellite galaxies, which have since then been disrupted in UDG1 and released their star clusters. The other scenario, perhaps a more natural one given the similar colors of the GCs (Danieli et al. 2022), is that the clusters may have formed in situ but in an extended configuration or with high velocity dispersion, e.g., during collisions of high-redshift gas clouds that belong to different satellite galaxies (Silk 2017; van Dokkum et al. 2022).

3.2. Burkert Halo

Figure 6 shows the posterior distributions with Burkert halos. The results are overall similar to those with an NFW halo, but with subtle, interesting differences. The mode values are $M_h = 10^{9.0} M_\odot$, $c = 25$ ($c_{-2} = 16$),[11] and $r_0 = 5.0$ kpc, and the medians with the 16th and 84th percentiles are $\log(M_h/M_\odot) = 9.8^{+0.4}_{-1.0}$, $c = 22^{+5}_{-9}$ ($c_{-2} = 14^{+4}_{-6}$), and $r_0 = 3.4^{+1.1}_{-1.4}$ kpc. The mode halo mass is similar to that of the NFW case, both of which leave the galaxy in the relatively DM-poor territory with respect to the stellar-mass–halo-mass relations (e.g., Behroozi et al. 2013). The concentration is significantly higher, within 1σ of cosmological concentration–mass relations (e.g., Dutton & Macciò 2014), but is still on the lower side for its halo mass. The median halo mass is higher, making the galaxy less extreme in terms of the stellar-to-halo–mass ratio.

For the Burkert halo, the degeneracy between concentration and halo mass is weaker. Again, this can be understood using the proxy of DF strength, $\rho(r)/V^2_{\rm circ}(r)$ —while, in the NFW case, increasing both c and M_h can increase this quantity for the radius range of interest ($r \lesssim 5$ kpc); it is no longer the case with a Burkert profile. Instead, the $\rho(r)$ changes when varying c almost exactly cancels that in $V^2_{\rm circ}$. This is also why the constraining power on halo concentration is rather weak. For the initial scale distance r_0, we also obtain a median value that is larger than the effective radius of UDG1, so the same formation scenarios could be hypothesized.

Similarly, we generate a model realization of 300 GCs with the mode parameters of the Burkert halo, and as shown in Figure 7, it also reproduces most aspects of the data. Hence, either a cuspy halo or a cored halo can more or less reproduce the observed GC statistics. There is a weak but noticeable difference, that more GCs can reach smaller distances in a Burkert host: in the R–m plane, very few model GCs with $m \sim 10^5 M_\odot$ populate the region of $R \lesssim 1$ kpc in the NFW host, but, here, there is a more significant low-R tail. The same trend was actually also seen in Bar et al. (2022), which adopted a simpler model and ignored the details of GC evolution. The most obvious difference that the different profile shapes can cause is actually the fraction of GCs that reach the center of the host galaxy and form an NSC. We will discuss this further in Section 4.

[11] Halo concentration usually refers to $c_{-2} = r_{\rm vir}/r_{-2}$, with r_{-2} the radius at which the logarithmic density slope is -2. The NFW scale radius r_s is the same as r_{-2}, but the Burkert scale radius $r_s (= r_{\rm vir}/c)$ is $r_{-2}/1.52$, so the Burkert concentration c quoted here is 1.52 times the c_{-2} as commonly reported in cosmological concentration–mass–redshift relations.

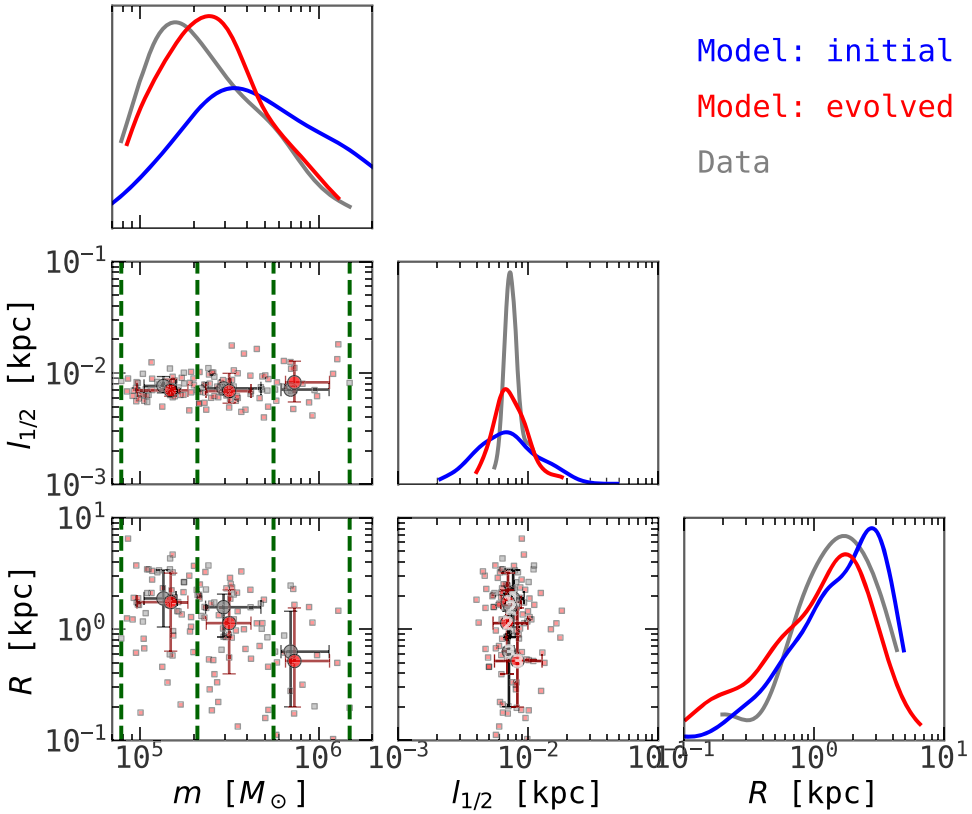

Figure 5. Model realization with an NFW host halo and the mode parameters ($M_h = 10^{9.10} M_\odot$, $c = 4.08$, and $r_0 = 3.14$ kpc) compared to the data. The diagonal panels show the (individually normalized) one-point functions of star–cluster mass m, size $l_{1/2}$, and galactocentric distance R. The red circles stand for the median model predictions in the three mass bins (whose boundaries are indicated by the vertical dashed green lines), while the gray circles are those from observation. The error bars indicate the 16th and 84th percentiles. The numbers i shown in the center of the circles in the $R - l_{1/2}$ plane mean that this point is for the ith mass bin.

3.3. Comparison with Scaling Relations

With the aforementioned halo–profile constraints, UDG1 is an outlier in several scaling relations of galaxy–halo connection and halo structure. First, for more massive galaxies, the abundance of GCs, N_{GC}, is an excellent indicator of the host virial mass (Harris et al. 2017): a simple linear relation, $M_{vir} = 5 \times 10^9 M_\odot \times N_{GC}$, fits the observational median for almost 5 decades in halo mass from $M_{vir} \sim 10^{10} M_\odot$ to $10^{15} M_\odot$. The scatter of this relation increases toward the lower-mass end, $\sigma_{\log N_{GC}} \propto M_{vir}^{-1/2}$, and is approximately 0.31 dex at $M_{vir} = 10^{11} M_\odot$ (Burkert & Forbes 2020). This relation has been widely used as a halo–mass estimator (e.g., Forbes et al. 2021) and was the basis of the hypothesis that some of the most GC-abundant UDGs are failed L^* galaxies (e.g., van Dokkum et al. 2016). If we assume for simplicity that the scatter in virial mass at a fixed GC abundance is the same as that in the GC abundance at fixed mass, i.e., $\sigma_{\log M_{vir}} = 0.31$, at $N_{GC} = 20$ and $\sigma_{\log M_{vir}} \propto N_{GC}^{-1/2}$, then a galaxy with 50 GCs is expected to have a virial mass of $M_{vir} = 10^{10.7 \pm 0.2} M_\odot$. Hence, according to our halo–mass estimates, UDG1, with a virial mass of approximately $M_{vir} \sim 10^{8.6-10.2} M_\odot$, is a dramatic outlier to this empirical N_{GC}–M_{vir} relation (as extrapolated to the lower-mass range) by several σ. We illustrate this in the upper panel of Figure 8. Here, the gray band actually represents the full width of the distribution of the observational sample compiled by Burkert & Forbes (2020)—despite the increase of the scatter at the low-mass end, UDG1 is still an outlier.

However, the N_{GC}–M_{vir} relation is based on massive galaxies, so the extrapolation to the low-mass end

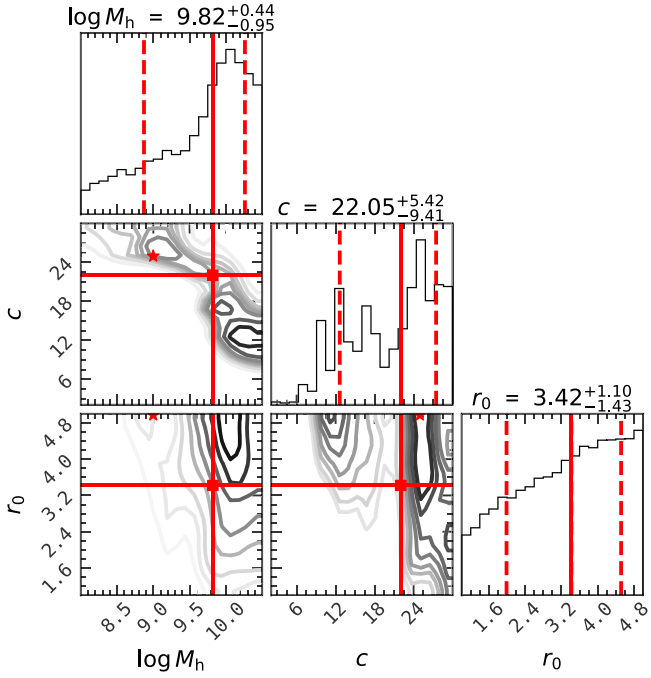

Figure 6. The same as Figure 4, but assuming a Burkert host halo.

($M_{vir} \gtrsim 10^{10} M_\odot$) is ungrounded, and the scatter of the relation may contain systematics with morphology. In fact, as Burkert & Forbes (2020) already noticed, in their effort of explaining this relation with halo merger trees, the relation must flatten at $M_{vir} \lesssim 10^{10} M_\odot$ or $N_{GC} \lesssim 100$, which is exactly the regime of

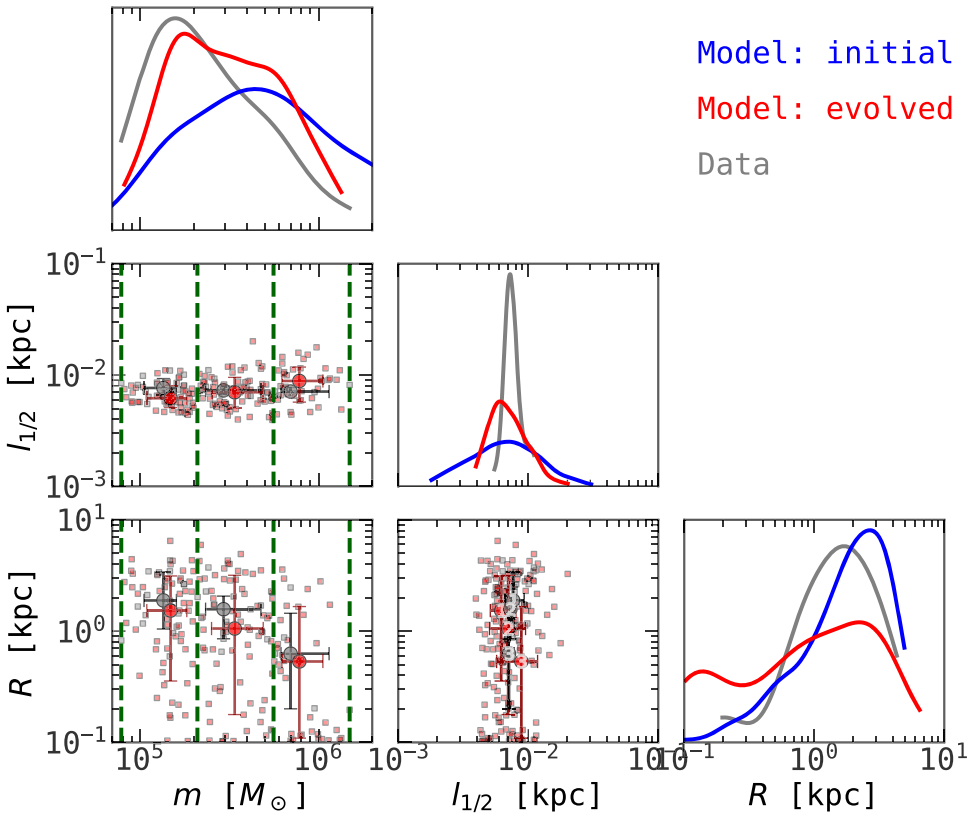

Figure 7. The same as Figure 5, but for the best-fit Burkert halo $M_{\rm h} = 10^{9.0} M_\odot$, $c = 25$ ($c_{-2} = 16.4$), and $r_0 = 5.0$ kpc.

GC-rich UDGs. This flattening is supported by the observational sample of dwarf galaxies whose virial masses are individually constrained with gas kinematics (Forbes et al. 2018), as represented by the gray band in Figure 8. Our virial–mass estimate of UDG1 is qualitatively in line with the flattening of the $N_{\rm GC}$–$M_{\rm vir}$ relation at the low-mass end, but more extreme, highlighting the danger of naively inverting the relation to infer the virial mass with the number of GCs.

Second, UDG1 is also an outlier to the stellar-mass–total-mass relation from abundance matching especially if assuming an NFW halo, as illustrated in the middle panel of Figure 8. For comparison, we have chosen the median relation as in Behroozi et al. (2013), and the recent estimate of the low-mass-end scatter using the dwarf satellites in the ELVES sample (Danieli et al. 2023). We caution that, despite being intensively studied, the low-mass end of the relation remains highly uncertain, and different assumptions lead to different results (see, e.g., Danieli et al. 2023, and the references therein). Our particular choice here is among the most flat for the low-mass-end median slope and among the largest in the scatter—even with these conservative choices, UDG1 is a $\sim 2\sigma$ outlier if assuming an NFW halo.

Third, as the bottom panel of Figure 8 shows, UDG1 stands out with respect to the concentration–mass relation of DM halos if the halo density profile is NFW. For comparison, we have shown a median c_{-2}–$M_{\rm vir}$ relation from cosmological N-body simulations (Dutton & Macciò 2014), with a constant scatter of 0.3 dex assuming a log-normal c_{-2} distribution at fixed $M_{\rm vir}$ (Diemer & Kravtsov 2015; Benson 2020).[12] Obviously, assuming an NFW halo, the UDG1 halo is significantly less concentrated than what is expected cosmologically for its mass. The concentration is within 1σ of the concentration–mass relation if the halo has a Burkert profile, but is still lower than the median relation. Overall, this is consistent with the scenario that UDG formation results from repeated supernovae feedback, which makes both the halo less concentrated and also the stellar distribution puffy (e.g., Jiang et al. 2019; Freundlich et al. 2020).

In short, the UDG1 DM halo stands out as a $\sim 2\sigma$ outlier compared to all the aforementioned scaling relations, especially when assuming an NFW profile. It is in line with the understanding that there is huge scatter in these relations at the low-mass end, and warns us against generalizing these relations to extreme galaxies and using them as virial mass estimators. We caution that our halo mass estimates for UDG1 are based on the assumption of a static host halo, whereas in reality the UDG1 halo might be a satellite of the galaxy group NGC5846, and thus have been environmentally processed. It may also have internally driven evolution due to supernovae feedback. To consider the host halo of UDG1 as a subhalo evolving in mass and structure is beyond the scope of this work, but it is reasonable to speculate that the peak virial mass of the system in the past is higher than our estimates here, and thus brings the system closer to the empirical scaling laws.

4. Discussion

In this section, we first discuss a few observational implications, including the line-of-sight (LOS) velocity dispersion of the GCs in UDG1, the orbital eccentricity distribution of the GCs, the stripped mass fraction of the GCs, and the fraction of NSCs. Second, we compare our model with that of the previous work of Bar et al. (2022), Modak et al. (2023).

[12] The scatter in principle varies with mass and the selection of halos based on whether they are relaxed, and 0.3 dex is a ballpark estimate.

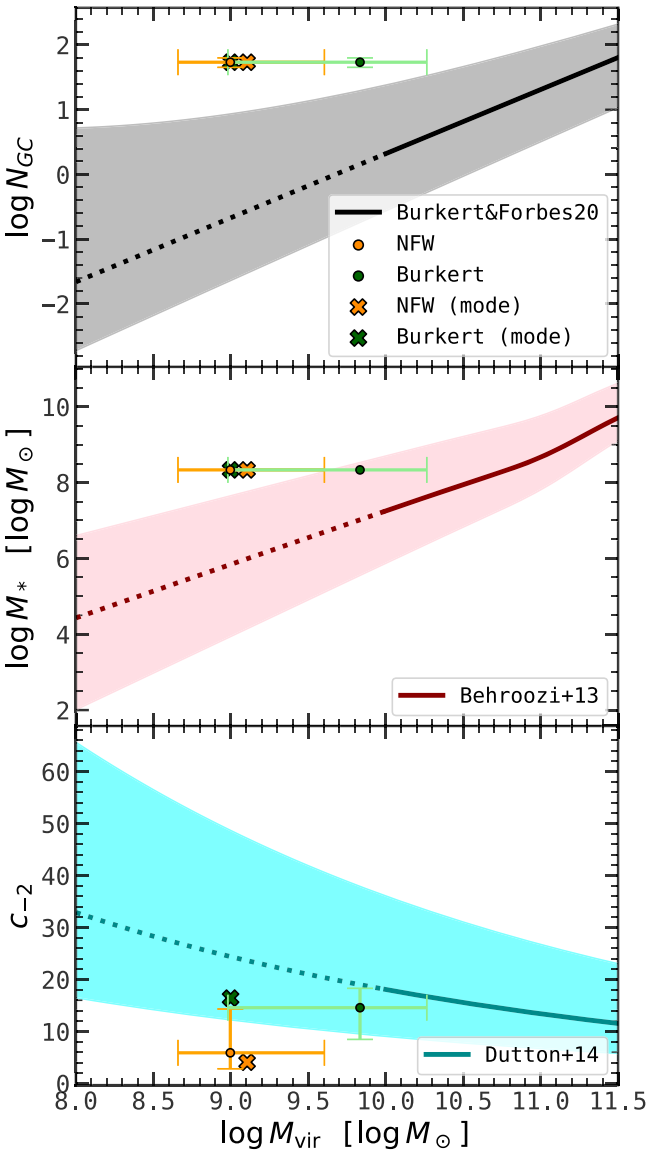

Figure 8. NGC5846-UDG1, with its DM halo constrained with the GC statistics, in comparison with the empirical scaling relations of GC number N_{GC} vs. virial mass M_{vir} (upper), stellar mass $M_\star$ vs. virial mass M_{vir} (middle), and halo concentration c vs. virial mass M_{vir} (bottom). The orange/green circles with error bars represent the medians with the 16th and 84th percentiles, and the crosses of corresponding colors represent the mode values, assuming NFW/Burkert halo. The lines stand for the median relations from Behroozi et al. (2013), Burkert & Forbes (2020), and Dutton & Macciò (2014). The dashed parts of the lines indicate extrapolations to a lower-mass range than that of the observational or simulation samples from which these relations are extracted. The gray band in the upper panel represents the full scatter of the observational sample as in Burkert & Forbes (2020). The red band in the middle panel indicates the 1σ scatter in $\log M_\star$ at fixed virial mass, as constrained using dwarf satellites in the ELVES sample, from Danieli et al. (2023). The cyan band indicates the 1σ scatter of 0.3 dex, assuming log-normal distributions of c at fixed virial masses. UDG1 is an outlier to these scaling laws by $\sim 2\sigma$–3σ.

Finally, we comment on the simplifications in this work, and point out potential future improvements and applications of our method. We explore the possibility of an initial mass segregation in Appendix D.

4.1. Velocity Dispersion and Orbital Eccentricity of the GCs

In the upper panels of Figure 9, we present the LOS velocity–dispersion profile of the evolved GCs in halos of the best-fit parameters. The dispersion profiles in the Burkert halo and in the NFW halo are similar, and, in comparison with that of smooth stars, which reflect the equilibrium kinematics of the host potential, both show a significant decrease, more so at smaller R. This is another manifestation of DF, besides mass segregation. Observationally, Müller et al. (2020) have measured the velocities of 11 of the member GCs of UDG1, and inferred a dispersion of $\sigma = 9.4^{+7.0}_{-5.4}$ km s^{-1}, at $R \approx 1.8$ kpc (i.e., the average distance of the 11 GCs to the galaxy center), assuming a simple pressure-supported spherical system. Our model predictions agree with this measurement. In fact, a closer examination of the posterior distribution of the GC velocity dispersion of Müller et al. (2020) reveals that the mode value is approximately 8 km s^{-1}, almost exactly on top of our NFW model results.

Interestingly, however, Forbes et al. (2021) measured the velocities of the smooth stellar distribution of UDG1 using KCWI on the Keck telescope, and found a rather high value of the smooth-star velocity dispersion of $\sigma_\star = 17 \pm 2$ km s^{-1}, higher than the equilibrium value ($\sigma \sim 11$ km s^{-1}) of a low-mass ($M_{vir} \sim 10^9 M_\odot$) and extremely low-concentration system as advocated by our best-fit NFW cases, and more consistent with a virial mass of $M_{vir} \sim 10^{9.5-10} M_\odot$ and of normal concentration as in the Burkert cases. In none of the models explored here, we reproduce such a large difference between the GC dispersion and the smooth-star kinematics. We opt not to dive into the factors that may reconcile the tension, such as oversimplifications in our model or nonequilibrium of the stellar distribution. Instead, we can see that these two observational studies together (Müller et al. 2020; Forbes et al. 2021) present a qualitatively similar picture as what our model reveals here, i.e., the GCs of UDG1 have smaller velocity dispersion than the smooth stars, indicative of DF, and the virial mass of UDG1 is lower than what is expected from the scaling laws.

The different GC dynamics with the two halo profiles may result in different orbital eccentricities of the GCs. As shown in the lower panels of Figure 9, while the orbital eccentricity distributions are initially similar (which is by construction, because we assumed isotropic velocity distribution in both cases), evolution in the Burkert host makes the orbits slightly more eccentric. This effect actually only operates on the GCs whose initial apocenter is larger than the core radius and whose initial pericenter is below the core radius. Such GCs experience DF only at the apocenter but not at the pericenter because of core-stalling—this makes the orbits more radial. Note that DF will otherwise not affect orbital eccentricity, a counterintuitive behavior already discussed in van den Bosch et al. (1999), because the eccentricity decreases near pericenter but increases again near apocenter.

4.2. Nucleated Ultra-diffuse Galaxies

A significant fraction of UDGs are nucleated, in the sense that they feature a compact stellar distribution at or near the geometric center of the system (Greco et al. 2018; Lim et al. 2018; Iodice et al. 2020; Marleau et al. 2021). The compact stellar source, also known as the NSC, is more compact than a stellar bulge as in an early-type galaxy and is more massive than a typical GC—imaging samples can be found in Lim et al. (2018; Figure 3). The fraction of UDGs that are nucleated is approximately 30%–40% in nearby galaxy clusters, and seem to show an environment dependence such that the fraction is

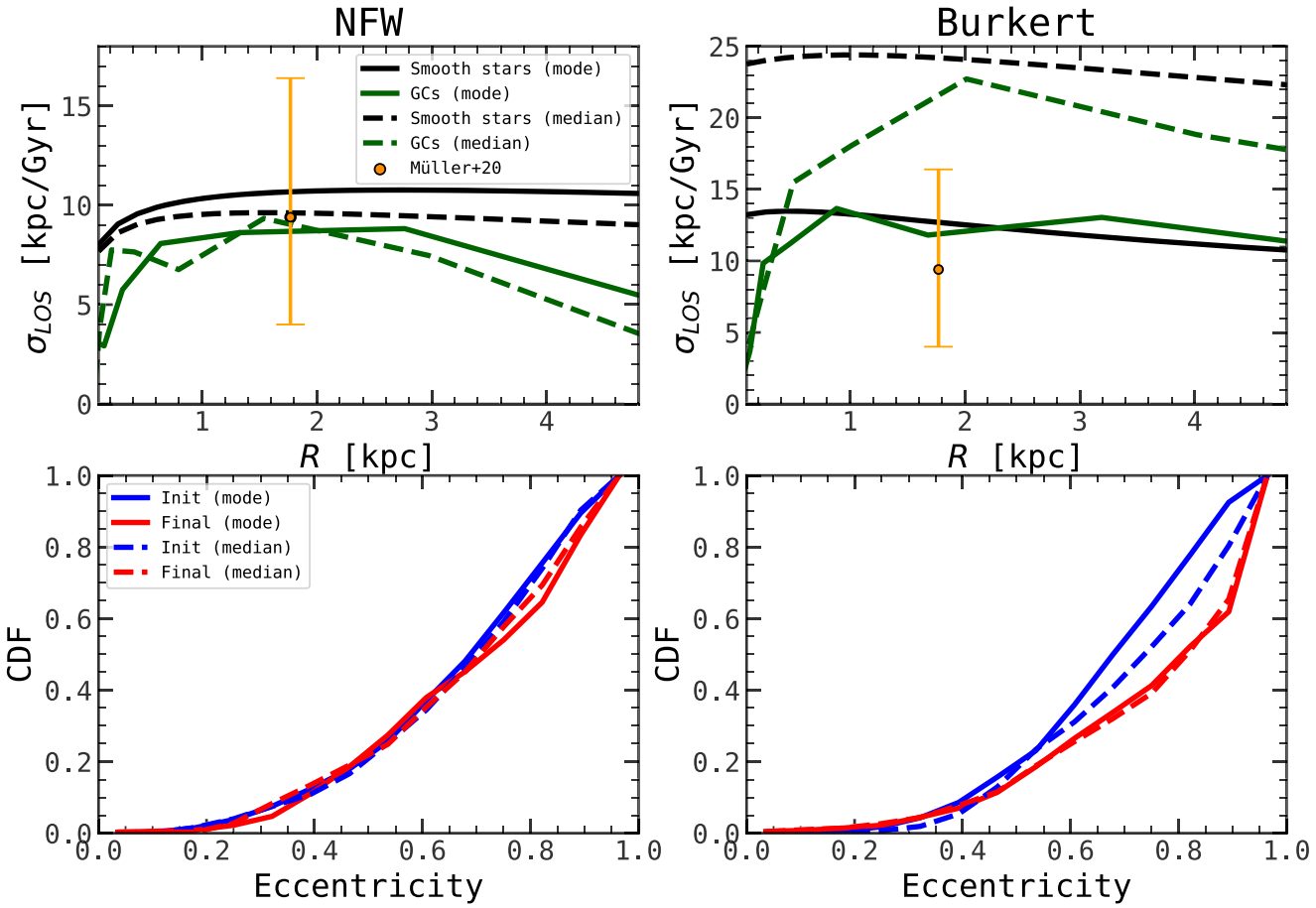

Figure 9. Upper panels: LOS velocity–dispersion profiles of the GC population in comparison with that of the smooth stars. Lower panels: cumulative distributions of orbital eccentricity of the star clusters. The left column represents the result for NFW halo while the right column represents the result for Burkert halo. The solid lines represent our best-fit model results while the dashed line represents our median model results. In the upper panels, black lines stand for smooth stars, and green lines stand for evolved GCs. In the lower panels, red lines stand for the final stage, and blue lines stand for the initial distribution, and the line style differentiates the mode and median results, respectively. The orange circle with error bar is inferred from the observed kinematics, based on about one-fifth of all the ∼50 member GCs (Müller et al. 2020).

higher in the densest region and decreases toward the outskirts of the galaxy cluster (Lim et al. 2018).

It is natural to attribute the formation of an NSC to the coalescence of the GCs that have lost their orbital angular momentum completely due to DF and sunk to the center. If this is the case, we can expect that different DM profiles, as well as different initial GC distributions, can determine the nucleatedness of a UDG and the mass of the NSC. Modak et al. (2023) already showed that NSCs only form in cuspy halos and almost never form in a cored halo. Here, we revisit this scenario using our model, which is more refined in terms of GC evolution compared to the previous work. We emphasize that this experiment is for GC-rich dwarfs in general, no longer aimed at reproducing UDG1. We quantify the nucleatedness of the resulting system using the mass fraction of the nucleus, $f_{\rm nucleus}$, defined as the total mass of the GCs that settle to $r < 0.1$ kpc, divided by the total mass of all the GCs.

Figure 10 shows $f_{\rm nucleus}$ as a function of halo mass $M_{\rm h}$, halo concentration c, and the initial Hernquist scale of the GC distribution r_0. Here, a cuspy NFW profile and a cored Burkert profile exhibit a dramatic difference, in the sense that the nucleus fraction in a cored halo is usually much lower (except for the combination of the lowest $M_{\rm h}$, highest c, and largest r_0, which happens to be our best-fit case), whereas that of a cuspy halo is usually much higher, especially when the halo mass is below $M_{\rm h} \sim 10^{9.5} M_{\odot}$. The generally low nucleus fractions of a cored halo are due to the stalling effect, which prevents the GCs from dropping deeper (see Banik & van den Bosch 2022, for a thorough discussion) and is empirically captured by the Petts et al. (2015) prescription adopted here. However, in our best-fit Burkert profile, which has a fairly high concentration, while there is a flat core in the very center, the density is still steeply rising toward the center in the radius range where most GCs are. The inset of Figure 10 compares the best-fit NFW and Burkert profiles: we can see clearly that the Burkert profile is even steeper than the NFW counterpart at the initial Hernquist scale radius for the GC distribution. It is this steep density slope at the regime where the GCs populate that gives rise to sufficiently strong DF and therefore mass segregation. Otherwise, if the core radius is larger than where the star clusters are, there will be no mass-segregation trend, and, for the same reason, no NSC forming.

There are trends of the nucleus fraction with the model parameters. First, a larger halo mass leads to smaller $f_{\rm nucleus}$. This is because of the dependence of the DF strength on the mass ratio between the GC and the host. Second, and intuitively, a larger scale length leads to smaller $f_{\rm nucleus}$, since if GCs start out at large distances, they need stronger DF or longer time to sink to the center. Third, as to the concentration dependence, for NFW halos, a higher concentration leads to a

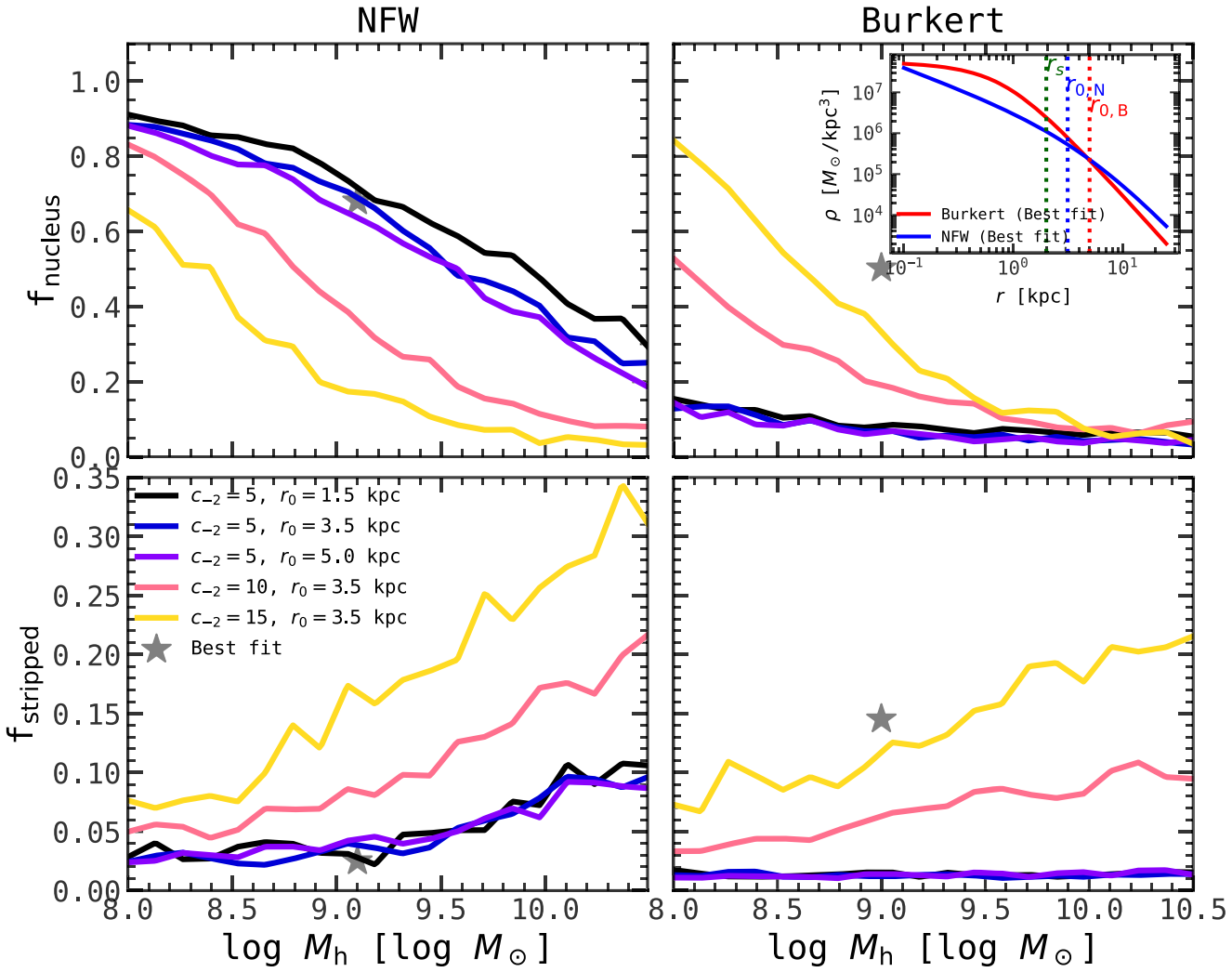

Figure 10. Upper panels: the mass fraction of nuclear star cluster (the total mass of the GCs that have sunk to the center of the galaxy due to DF, divided by the total mass of all the GCs in the galaxy) as a function of halo mass. Lower panels: The stripped fraction of GCs (the total mass difference between GCs in beginning and in final stage, divided by the total mass of all the GCs in the galaxy) as a function of halo mass. The left and right columns show the results assuming cuspy (NFW) and cored (Burkert) profiles, respectively. Different colors represent different combinations of the halo concentrations (c) and the scale length (r_0) of the initial GC distribution, as indicated. The inset panel shows the density profile of NFW halo (red solid line) and Burkert halo (blue solid line) with best-fit parameters. The vertical green dotted line represents effective radius of the galaxy while the blue dotted line and red dotted line stand for the best-fit initial GC scale radius for NFW case and Burkert case, respectively.

lower $f_{\rm nucleus}$, at fixed halo mass. This, again, can be attributed to the competing effects on DF from c and $M_{\rm h}$, as we discussed in the context of the c_{-2}-$M_{\rm h}$ degeneracy of a cuspy halo in Section 3.1. For Burkert halos, the c_{-2}-trend is vague, and can similarly be attributed to the null effect of varying c_{-2} on the DF acceleration as we argued in Section 3.2, unless the halo mass is sufficiently low such that a higher c_{-2} makes the regime of steep density slope overlapping with the GCs. The difference in the nucleus fraction between the cuspy and cored cases implies the possibility of using NSCs to infer the DM distribution of UDGs, and could be further explored in future statistical studies.

4.3. Stripped Fraction of GCs

A higher host–halo density will lead to more tidal stripping of star clusters, as can be expected from Equation (11). Hence, naturally, a positive correlation exists between halo concentration and the stripped mass fraction of the GCs, as shown in the lower panels of Figure 10. For the same reason, when concentration is fixed, a more cuspy halo results in more stripped mass from the star clusters—this can be seen by comparing the NFW and Burkert results in the lower panels of Figure 10.

However, if we limit the scope of comparison to the halos that can produce the observed mass segregation, we get the seemingly counterintuitive result that, in the best-fit NFW case, the stripped fraction of the GCs is marginal, whereas, in the best-fit Burkert model, the GCs have contributed a fairly large fraction ($\gtrsim$10%) of their masses to the smooth stars. This is simply because the best-fit Burkert halo is actually denser in the regime where most of the GCs exist ($r\lesssim r_0$), as shown by the inset of Figure 10.

Note that the star clusters that have been completely disrupted also deposit their mass to the smooth-star reservoir. It is an interesting question whether UDGs obtain a significant (or even dominant) fraction of their smooth stellar mass from stripping as well as from disrupted star clusters (e.g., Danieli et al. 2023). However, since the fraction of completely dissolved star clusters depends sensitively on the $M_{\rm min}$

parameter of the ICMF, and $M_{\rm min}$ is not a parameter that we have sufficient constraining power based on radial mass segregation, we cannot make a conclusive argument on this scenario.

4.4. Comparison with Previous Studies

Bar et al. (2022) also studied the mass segregation of GCs in UDG1 using a semianalytical model of similar nature to ours. Modak et al. (2023) studied GC statistics in a more compact dwarf galaxy but adopted a very similar model to that of Bar et al. (2022). There are a couple of major improvements here in our approach.

First, the previous studies did not trace the mass and structural evolution of GCs along the orbits, but instead adopted, e.g., as in Bar et al. (2022), a simple empirical model of GC mass loss, $m(t) = m(0)(1 - \delta t/t_0)$, with $\delta = 0.3$, $t_0 = 10$ Gyr, for all the GCs. That is, the mass evolution is linear with time, irrespective of the local tidal field, and there is no structural evolution. Modak et al. (2022) makes the mass evolution exponential, but the other aspects remain the same. Related, the GC mass distribution in these works was manually set to match that observed. As discussed in Section 2, the mass and structural evolution affects the DF strength, via the Coulomb logarithm, and thus, the orbit evolution could be different if the mass or size is not properly accounted for. In our model, the GCs evolve self-consistently in mass and structure under the influence of tidal effects and two-body relaxation. Besides, the evolution starts from theoretically motivated or observationally motivated initial mass functions and initial structural distributions. As such, besides the GC mass-segregation signal, the evolved GC mass function and size–mass relation are also emergent predictions in our model, and, as demonstrated, they both agree decently with the data.

Second, the previous studies did not aim at statistically constraining the DM halo mass or structure. Instead, they adopted a couple of somewhat arbitrary fixed halo masses and profiles, and tested whether mass segregation could arise under these somewhat arbitrary choices. For example, Bar et al. (2022) used an NFW host with $M_{\rm h} = 10^{9.78} M_\odot$, and $c_{-2} = 6$ and a Burkert host, with $M_{\rm h} = 10^{9.53} M_\odot$, and $c_{-2} = 15.4$. Basically, their halo masses are approximately 0.5–1 dex higher than what we found here, and their halo concentrations happen to be in the same ballpark with our posterior-mode values. Interestingly, however, they could achieve mass segregation with these more massive halos, whereas our model cannot.

The main factor that causes the difference lies in the star–cluster evolution—with our model, mass loss depends on the instantaneous internal and external conditions, such that the clusters getting closer to the host center experience stronger mass loss. This counterbalances the mass-segregation effect of DF. Hence, to obtain mass segregation with our model, stronger DF is needed, which translates to a lower halo mass because of the dependence of DF on the perturber-to-host mass ratio. This is illustrated in Figure 11, where we keep the host halo as well as the initialization of coordinates and velocities the same, and evolve the star clusters using the Modak et al. (2023) model and our model, respectively, for results shown in the left and right panels. The mass initialization cannot be exactly the same because of the difference in the evolution prescriptions, but we have adjusted the ICMF to make the evolved mass distributions comparable. As can be seen, with the Modak et al. (2023) model, significant mass segregation can already be produced for a relatively massive NFW host halo of $M_{\rm h} = 10^{10} M_\odot$, while our model produces a marginal trend for this mass. For the lower halo mass of $M_{\rm h} = 10^{9} M_\odot$, both models can produce similarly strong mass segregation.

Another factor here is that the previous studies did not follow star–cluster structural evolution. As we already discussed, neglecting the size results in a larger Coulomb logarithm and thus stronger DF. In short, it is easier to get mass segregation with the Modak et al. (2023), Bar et al. (2022) models, because the mass loss is orbit-independent, and because DF is stronger when neglecting the cluster size. It is therefore important to model GC evolution accurately for the purpose of constraining DM distribution.

4.5. Simplifications and Future Work

While in this work we have improved upon previous studies by introducing a self-consistent physical model of GC evolution and employing MCMC to constraint the DM halo properties, we caution that there are still oversimplifications that leave room for future improvements. Addressing them quantitatively is beyond the scope of current work, but, here, we point out qualitatively how they might affect the results and sketch ideas for future studies. The discussion applies not just to the specific galaxy UDG1, but to GC-rich dwarf galaxies in general.

First, we have assumed that the host potential is static over the entire evolution of the GC population. However, UDG1 is a satellite galaxy of the galaxy group NGC5846, and many GC-rich low-surface-brightness galaxies are members of galaxy groups or clusters. That is, the host halo of UDG1 may be a subhalo that has experienced significant mass loss if it had orbital pericenters sufficiently close to the center of the host group. In this case, UDG1 may lie closer to the scaling relations (Section 3.3) if its peak virial mass and the concentration at the peak mass are used in place of the present-day values. In fact, it has been argued that the differential tidal mass loss between the subhalo and the stellar component can produce DM-deficient dwarf galaxies (Moreno et al. 2022). Even for an isolated dwarf galaxy, the host halo is not static, but increases in mass gradually. It is in principle possible to parameterize the mass assembly history of the host halo or subhalo using empirical models extracted from cosmological simulations (e.g., Wechsler et al. 2002). However, this would introduce additional model parameters that need to be marginalized over, not to mention that there is significant halo-to-halo variance in the mass histories (Jiang & van den Bosch 2017) so that a certain choice of the parameterization may not be representative. A more viable way of exploring statistically the effect of a dynamic host is to postprocess cosmological numerical or semiananlytical simulations and populate simulated halos with GCs and study the GC statistics. We leave this idea to a future study.

Second, there are a few other mechanisms for GC mass and structural evolution besides tidal interactions and two-body relaxation, including, among others, stellar evolution and gravothermal core collapse. Lamers et al. (2010) provide an empirical formula for mass loss of GCs due to stellar evolution obtained from collisional N-body simulations. Following their model, GCs lose $\sim$25% of their initial mass over 10 Gyr, insensitive to their initial masses. Therefore, this effect can simply be offset by shifting the ICMF. The more complicated

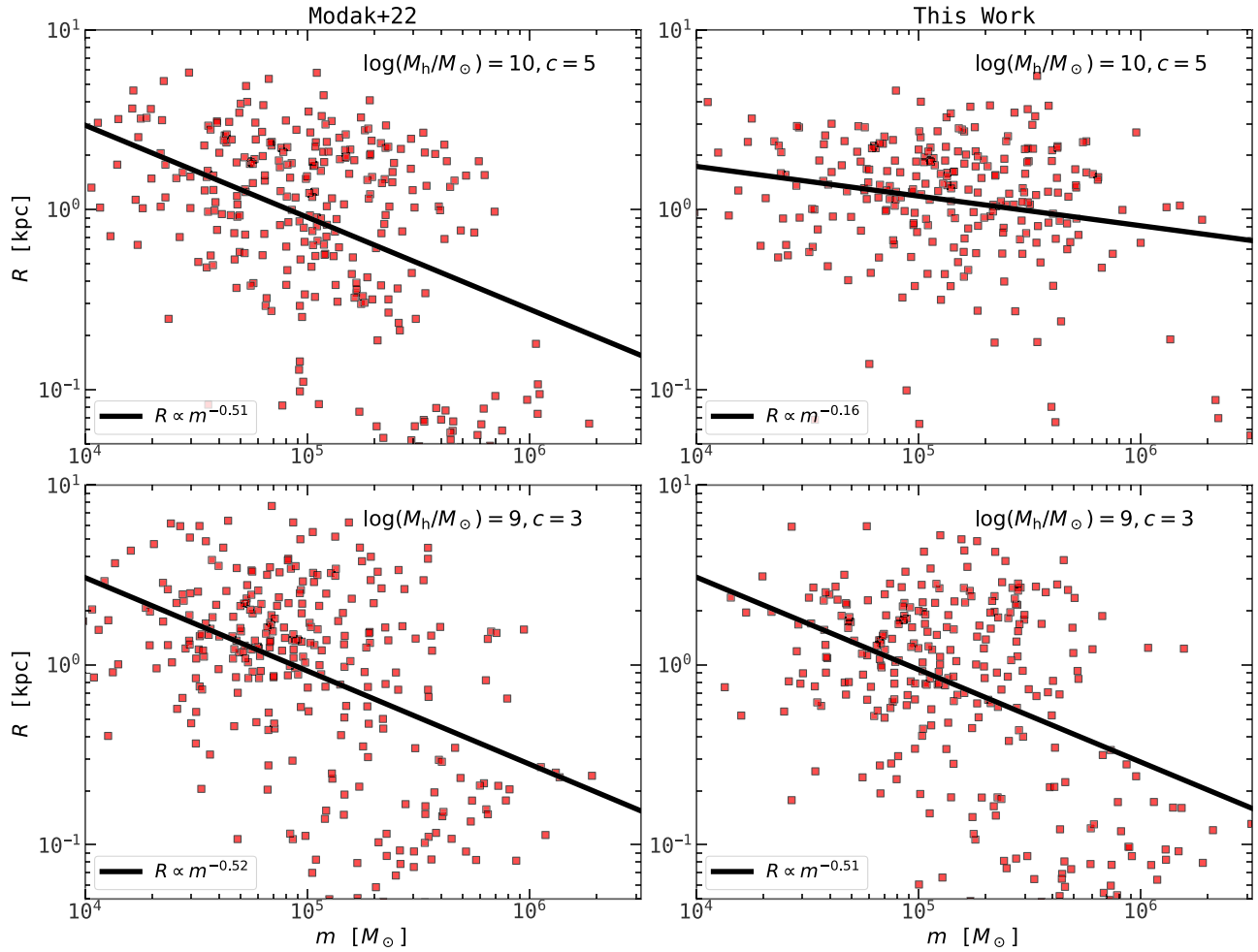

Figure 11. Illustration of the impact of the star–cluster evolution model on the halo mass at which GC mass segregation occurs: projected galactocentric distance vs. GC mass, in host halos of given mass and concentration, as quoted, obtained using the Modak et al. (2023) model (left) and the model presented in this work (right) with the same initialization scheme. To make the results statistically robust, 20 random realizations of 50 initial star clusters are included. Linear regression results are overplotted to gauge the strength of the mass segregation. Upper panels: with a relatively massive halo ($M_{\rm h} = 10^{10} M_\odot$), our model produces marginal mass segregation, while the Modak et al. (2023) model, featuring orbit-independent mass loss and neglecting star–cluster size in the DF treatment, can already produce fairly strong mass segregation. Lower panels: with a lower halo mass of $M_{\rm h} \sim 10^9 M_\odot$ and a low concentration, both models can produce rather strong mass segregation.

effect is the gravothermal core collapse of GCs, which steps in after when an isothermal core is established due to two-body relaxation. The core contracts since it is dynamically hotter than the outer part and transports energy to the outskirts. This makes the GC profile deviate from the EFF profile assumed in this work (or more generally, the King models), and become cuspy and resistant to tidal mass loss. The core-collapse timescale has been estimated to be 12–19 times the relaxation time $\tau_{\rm r}$ given in Equation (13) (Quinlan 1996), so it can be shorter than the Hubble time for the lower-mass GCs ($m \lesssim 10^{4.5} M_\odot$).

Third, if future kinematics observations can narrow down the DM profile, we can then adapt our model to constrain the other model ingredients. For instance, while the ICMF is believed to follow the functional form of Equation (19), the power-law slope as well as the mass scales are not fully constrained and likely exhibit variation from one population to another (see, e.g., Alexander & Gieles 2013, for a discussion on the power-law slope). It would be interesting to treat the ICMF parameters as free parameters, and combine the GC evolution model and the MCMC method as in this study to constrain the ICMF, to investigate, for example, whether UDGs have a unique ICMF.

5. Conclusion

In this work, we are motivated by a remarkable ultra-diffuse galaxy, UDG1, whose globular-cluster population exhibits interesting radial mass segregation, and aim to explore the possibility of reproducing the mass segregation of the GCs with DF and constraining the DM content of the UDG using photometric data alone. To this end, we have introduced a simple semianalytical model that describes the evolution of GC populations in their host DM halo and galaxy, accounting for the effects of DF, tidal evolution, and two-body relaxation. We also consider educated assumptions of the initial properties of the GC progenitors, including the mass function, structure, and spatial distributions. We forward-model the GCs in a UDG1-like host potential (consisting of a DM halo and a smooth stellar distribution) to match the observed GC statistics from Danieli et al. (2022), and use MCMC to constrain the DM distribution (halo mass $M_{\rm h}$ and concentration c) of UDG1, as well as the scale radius of the initial star–cluster spatial distribution (r_0). While we have focused on UDG1, the methodology developed here is generally applicable to dwarf

galaxies in equilibrium with a rich GC population. We summarize our methodology and the main findings as follows.

We have shown that the orbital evolution under the influence of DF depends on the mass and structural evolution. Our model can self-consistently evolve the mass and structure of individual GCs along their orbits, capturing the effect of a varying tidal field along an eccentric orbit around the central region of a galaxy. In the limit of a weak tidal field, the mass and structural evolution in our model reduces to that of the classical work of Hénon (1965); while, in the limit when the timescale for tidal stripping is shorter than the two-body relaxation, the structural evolution follows that of the empirical tidal evolution track for collisionless systems of Peñarrubia et al. (2010) with cored density profiles, which applies to the assumed EFF density profiles of the GCs. Reassuringly, over the timescale of $\sim$10 Gyr, a population of star clusters drawn from reasonable ICMFs (Trujillo-Gomez et al. 2019) and initial structure–mass distributions (Brown & Gnedin 2021) evolves in a converging manner regarding its evolved mass and size distributions—notably, the lower-mass clusters ($m \lesssim 10^{4.5} M_\odot$) expand and get dissolved more easily, whereas the most massive clusters ($m \gtrsim 10^6 M_\odot$) remain largely intact, making the evolved GC mass function peak at $m \sim 10^5 M_\odot$ and the evolved GC size–mass relation flat, as observed.

No matter whether the density profile of UDG1 is cuspy or cored, we find that the DM halos that can give rise to the observed mass segregation are of low mass and low concentration. In particular, with an NFW (Burkert) halo, we obtained a posterior-mode halo mass of $M_{\rm h} = 10^{9.1} M_\odot$ ($10^{9.0} M_\odot$) and concentration of $c_{-2} \approx 4$ (16). There is a concentration–mass degeneracy (anticorrelation) in the case of an NFW profile, driven by the similar effects of increasing concentration and increasing mass on the DF strength in the central few kiloparsecs of the host potential. Given the stellar mass of UDG1 of $M_\star \sim 10^8 M_\odot$, these halo–mass estimates put UDG1 in the DM-poor territory.

In fact, UDG1 is an outlier compared to both the stellar-to-total-mass relation (e.g., Behroozi et al. 2013; Danieli et al. 2023) and the GC-abundance–total-mass relation (e.g., Harris et al. 2017; Burkert & Forbes 2020). The latter relation is known to flatten and increase in scatter at the low-mass end, and UDG1, with our halo–mass estimates, is in qualitative agreement with this trend, although more extreme. This warns against using this relation naively for halo–mass estimates for UDGs.

The estimated halo concentrations are lower than the cosmological average value expected for halos of the posterior masses. This lends support to the theoretical picture that UDGs populate low-concentration halos, which are puffed up by repeated supernovae outflows or environmental effects (e.g., Di Cintio et al. 2017; Chan 2019; Jiang et al. 2019). The posterior scale distance of the initial star–cluster distribution (which is assumed to follow an Hernquist profile) is $r_0 \sim 3$ kpc. Hence, the star clusters were likely in a more extended configuration initially than the (present-day) smooth stars, which has an effective radius of 2 kpc. This may imply that the star clusters are either of ex situ origin or formed in situ but in an extended configuration achievable via collisions of high-redshift gas clouds.

The radial mass segregation of GCs can be reproduced with either assumption of the halo profile, if we just focus on the distance–mass slope of the GCs that have not sunk to the center of the galaxy (Section 3). However, if we include all the GCs including the ones that have completely lost orbital angular momentum due to DF, and consider the NSC that forms out of GC mergers at the center of the galaxy, then the cuspy NFW halo can yield massive NSCs provided that the halo mass is below $10^{10} M_\odot$, whereas cored halos do not result in any significant NSC. Therefore, a viable formation mechanism for nucleated UDGs (e.g., Lim et al. 2018) is the orbital decay of GCs in a low-mass cuspy halo (see also Modak et al. 2023). As UDG1 seems to be a nonnucleated UDG, our results suggest that it is more likely to be hosted by a cored, low-mass DM halo. This is, again, in line with the theoretical picture that UDG formation goes hand-in-hand with the core formation of DM halos due to nonadiabatic perturbations of the gravitational potential.

Last but not the least, compared to the observationally costly kinematics measurements, our model can reproduce the observed LOS velocity dispersion of the GCs (Müller et al. 2020), and can reveal the difference between the velocity dispersion of the GCs and the smooth stellar background. This also manifests DF and is in qualitative agreement with what is observed (Forbes et al. 2021).

In summary, we have demonstrated with the case study of UDG1 that, as long as dwarf galaxies host a statistically significant number of GCs and the GCs form a radial mass trend, one can use a computationally efficient semianalytical model such as the one laid out in this work to constrain the hosting DM distributions. This is in principle feasible with imaging data alone. However, getting clean samples of GCs with little contamination from background galaxies or foreground stars requires deep, high-resolution imaging—this will soon be enabled by upcoming instruments, such as the Vera C. Rubin Observatory (LSST), the Chinese Survey Space Telescope (CSST), and Nancy Grace Roman Space Telescope (WFIRST).

Acknowledgments

F.J. thanks Avishai Dekel, Aaron Romanowsky, Frank van den Bosch, Hui Li, Kyle Kremer, Xiaolong Du, Ethan Nadler, and Jacob Shen for helpful general discussions. J.L. acknowledges the Tsinghua Astrophysics High-Performance Computing platform at Tsinghua University for providing computational resources for this work.

Software: `EMCEE` (Foreman-Mackey et al. 2013), `SatGen` (Jiang et al. 2021).

Appendix A
Analytics of Stellar Profiles and DM Halo Profiles

This section presents useful analytical expressions for the profiles we use in this work, including NFW (Navarro et al. 1997), Burkert (Burkert 1995), and a profile that describes the stellar density of UDG1. The density profiles are already given in the main text; here, we list the enclosed mass (M), gravitational potential (Φ), gravitational acceleration in the cylindrical coordinate system (f_R, $f_\phi = 0$, f_z), and the 1D velocity dispersion (σ) for an isotropic velocity distribution.

A.1. NFW

$$M(r) = M_{\rm h} \frac{f(x)}{f(c)}, \tag{A1}$$

where $x = r/r_s$, and $f(x) = \ln(1+x) - x/(1+x)$.

$$\Phi(r) = \Phi_0 \frac{\ln(1+x)}{x}, \tag{A2}$$

where $\Phi_0 = -4\pi G\rho_0 r_s^2$,

$$f_R = -\frac{\partial\Phi}{\partial R} = \Phi_0 \frac{f(x)}{x}\frac{R}{r^2}, f_z = -\frac{\partial\Phi}{\partial z} = \Phi_0 \frac{f(x)}{x}\frac{z}{r^2}, \tag{A3}$$

where $r = \sqrt{R^2+z^2}$.

$$\sigma^2(r) = -\Phi_0 x(1+x)^2 \int_x^\infty \frac{f(x')}{x'^3(1+x')^2}dx' \approx V_{\max}^2 \left(\frac{1.439x^{0.354}}{1+1.176x^{0.725}}\right)^2 \tag{A4}$$

where the second line is an approximation accurate to 1% for $x = 0.01$–100 (Zentner & Bullock 2003).

A.2. Burkert

$$M(r) = 2\pi\rho_0 r_s^3 g(x), \tag{A5}$$

where $\rho_0 = M_h/[2\pi r_{vir}^3 g(c)c^3]$, $g(x) = 0.5\ln(1+x^2) + \ln(1+x) - \arctan x$, and $x = r/r_s$.

$$\Phi(r) = \frac{\Phi_0}{4x}\left\{2(1+x)\left[\arctan\frac{1}{x} + \ln(1+x)\right] + (1-x)\ln(1+x^2) - \pi\right\}, \tag{A6}$$

where $\Phi_0 = -4\pi G\rho_0 r_s^2$.

$$f_R = -\frac{\partial\Phi}{\partial R} = \Phi_0 \frac{f_0}{x^2}\frac{R}{r_s}, f_z = -\frac{\partial\Phi}{\partial z} = \Phi_0 \frac{f_0}{x^2}\frac{z}{r_s}, \tag{A7}$$

where $r = \sqrt{R^2+z^2}$, and $f_0 = 2\arctan\frac{1}{x} + 2f(x) + 2\arctan x - \pi$.

$$\sigma^2(r) = -\frac{\Phi_0}{2}(1+x)(1+x^2)\int_x^\infty \frac{f(x')}{x'^2(1+x')(1+x'^2)}dx' \approx V_{\max}^{0.299}\frac{e^{x^{0.17}}}{1+0.286x^{0.797}}. \tag{A8}$$

A.3. UDG1 Stellar Profile

$$M(r) = \frac{M_\star}{2(9+2\sqrt{3}\pi)}[\sqrt{3}\pi + 18f_3(x) - 6\sqrt{3}f_2(x) + 9f_3(x)], \tag{A9}$$

where $x = r/r_s$ with r_s a scale radius ($r_s = 2$ kpc); and

$$f_1(x) = \ln\frac{1-x+x^2}{(1+x)^2}, \tag{A10}$$

$$f_2(x) = \arctan\frac{1-2x}{\sqrt{3}}, \tag{A11}$$

$$f_3(x) = \frac{x}{1+x}. \tag{A12}$$

$$\Phi(r) = \frac{\sqrt{3}\Phi_0}{54x}[(1+6x)\pi + 6(2x-1)f_2(x) + 3\sqrt{3}f_1(x)], \tag{A13}$$

where $\Phi_0 = -4\pi G\rho_0 r_s^2$.

$$f_R = -\frac{\partial\Phi}{\partial R} = \frac{\Phi_0 C}{54r^2}\frac{R}{x}, f_z = -\frac{\partial\Phi}{\partial z} = \frac{\Phi_0 C}{54r^2}\frac{z}{x}, \tag{A14}$$

where $C = \sqrt{3}\pi + 18f_3(x) - 6\sqrt{3}f_2(x) + 9f_1(x)$.

$$\sigma^2(r) = -\frac{\Phi_0}{54}(1+x)(1+x^3) \times \int_x^\infty \frac{\sqrt{3}\pi + 18f_3(x') - 6\sqrt{3}f_2(x') + 9f_3(x')}{x'^2(1+x')^2(1-x'+x'^2)}dx' \approx -\frac{\Phi_0}{54}\frac{1.845e^{x^{0.104}}}{1+0.563x^{1.158}} \tag{A15}$$

where the second line is an approximation specifically for UDG1.

Appendix B
GC Profile: EFF Profile

The EFF profile is specified by the total mass, m_{tot}, the scale length, a, and the power-law slope, η—the density profile is given by

$$\rho(l) = \frac{\rho_0}{(1+l^2/a^2)^\eta}, \tag{B1}$$

where

$$\rho_0 = \frac{\Gamma(\eta)}{\pi^{3/2}\Gamma(\eta-1)}\frac{m_{tot}}{a^3} \tag{B2}$$

is the central density, with $\Gamma(x)$ as the gamma function. The enclosed mass of EFF profile is given by

$$m(l) = \frac{4\pi}{3}l^3\rho_0 \mathcal{F}_{21}\left(\frac{3}{2}, \eta; \frac{5}{2}; -\frac{l^2}{a^2}\right), \tag{B3}$$

where $\mathcal{F}_{21}(a, b; c; z)$ is the hypergeometric function. By solving $m(l) = 0.5m_{tot}$, one can show that the half-mass–radius is given by

$$l_{1/2} = (2^{\frac{2}{2\eta-3}} - 1)^{1/2}a, \tag{B4}$$

a quantity that is repeatedly used in our model.

As mentioned in Section 2.2, to estimate the tidal heating parameter f_t, we have used the tidal evolution track of Peñarrubia et al. (2010) expressed in terms of the maximum-circular velocity v_{max} and the radius l_{max} at which v_{max} is reached. To this end, we need a relation between l_{max} and the parameters defining the profile, which is obtained as follows. The radius at which the circular velocity reaches maximum, l_{max}, is given by the solution of $dv_{circ}^2/dl = 0$, i.e.,

$$\mathcal{F}_{21}\left(\frac{3}{2}, \eta; \frac{5}{2}; -\frac{l^2}{a^2}\right) - \frac{3\eta}{5}\frac{l^2}{a^2}\mathcal{F}_{21}\left(\frac{5}{2}, \eta+1; \frac{7}{2}; -\frac{l^2}{a^2}\right) = 0 \tag{B5}$$

and is well approximated by

$$l_{max} \approx 1.825a \tag{B6}$$

for $\eta = 2$.

Appendix C
GC Mass–Distance Relations

As mentioned in Section 2.4, to facilitate the parameter inference, we precompute the model predictions of the observables used to construct the likelihood using 1000 GCs on a mesh grid spanned by the parameters of interest. We perform linear interpolation for model evaluations during the MCMC run.

Using the tabulated results, we plot the median relations between the evolved GC mass and distance for different halo mass $M_{\rm h}$ and different scale length r_0 of the initial star–cluster distribution, in Figures 12–13. The concentrations are kept

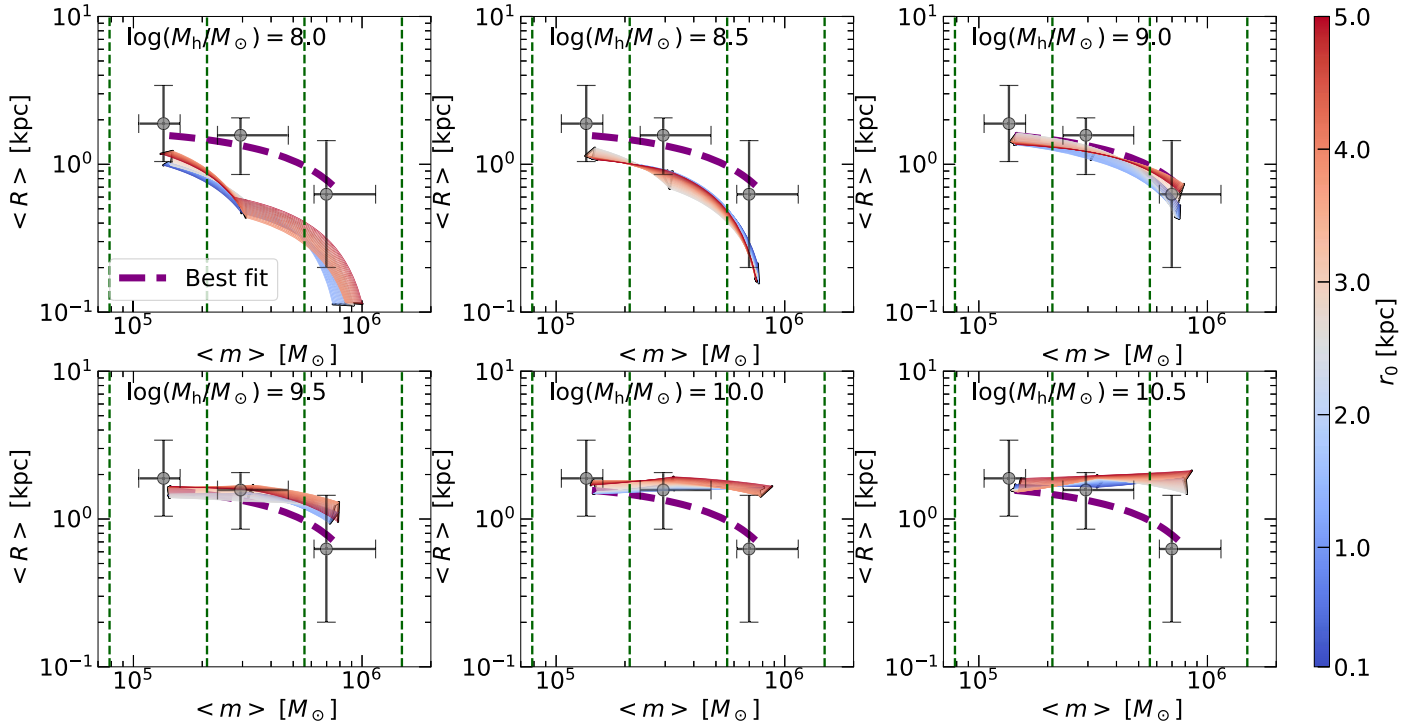

Figure 12. The median galactocentric distance $\langle R\rangle$ vs. the median GC mass $\langle m\rangle$, in three mass bins, for different host halo masses ($M_{\rm h}$) and different scale distance of the initial star–cluster distribution (r_0). The green dashed lines stand for the boundaries of the mass bins. The gray circles represent the data with the error bars indicating the 16th and 84th percentiles (the same across panels). The lines are model realizations for NFW halos with concentration $c = c_{-2} = 4$ fixed. The purple dash lines stand for the interpolation with the best-fit parameters.

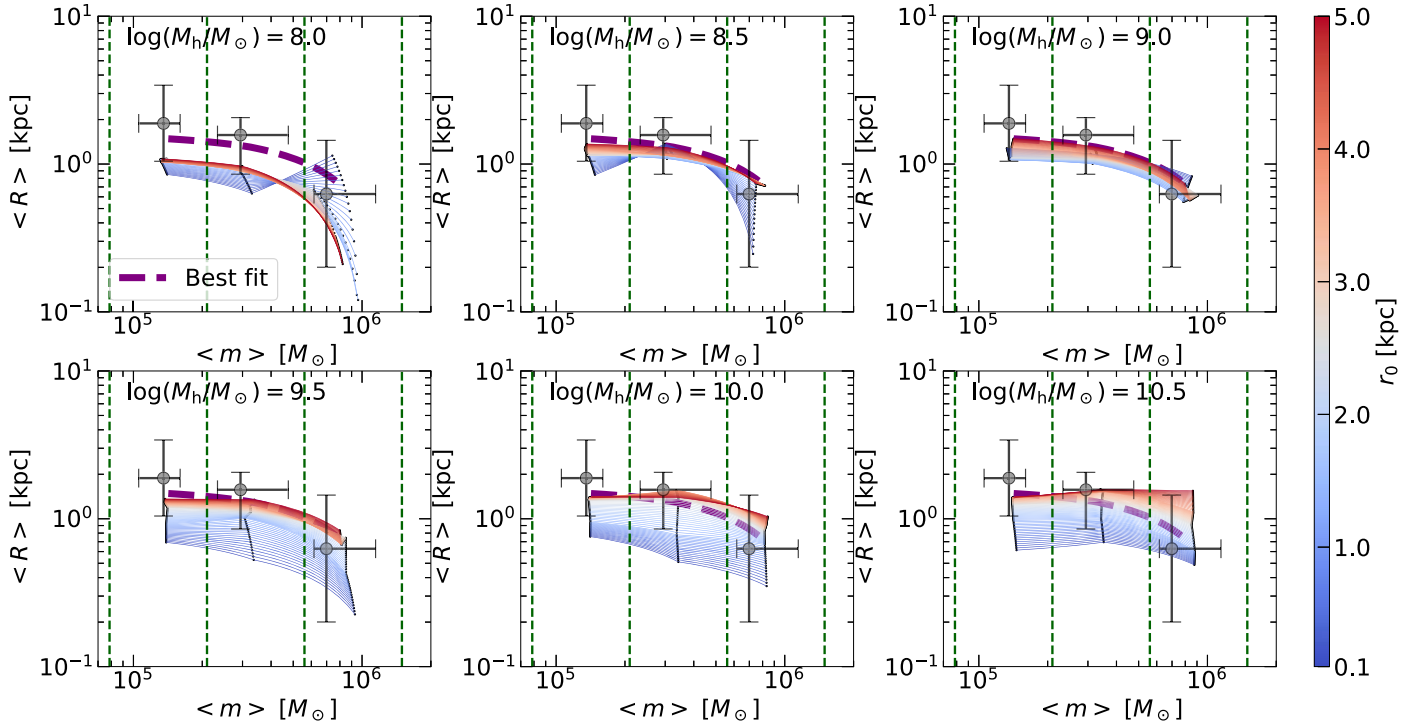

Figure 13. The same as Figure 12, but for Burkert halos with $c = 25$ ($c_{-2} = 16$).

fixed at the posterior-mode values, i.e., Figure 12 is for NFW halos of $c = c_{-2} = 4$, and Figure 13 is for Burkert halos of $c = 25$ ($c_{-2} = 16$). For the NFW case, we can see a clear mass segregation at $M_{\rm h} \lesssim 10^{9.5} M_\odot$, not very sensitive to r_0. For the Burkert case, the mass segregation is achieved at $M_{\rm h} \lesssim 10^{10} M_\odot$ but requires a relatively large r_0. In both cases, the halo mass cannot be too small ($\lesssim 10^{8.5} M_\odot$); otherwise, the median distances would be too small.

Appendix D
Effect from Initial Mass Segregation

Throughout this study, we have assumed that there is no mass segregation in the initialization. However, there might be mass segregation $\sim$10 Gyr ago if the molecular clouds that form GCs later had experienced DF already; or it might be that the gas–disk instability imprinted some primordial mass segregation. Here, we explore the effect of such an initial mass segregation. In particular, since our best-fit halo mass is low, we aim to qualitatively answer the question—what level of primordial mass segregation can give rise to the final observed segregation strength, in a halo that is significantly more massive than our posterior-mode masses and thus yields a much weaker DF effect.

In Figures 14 and 15, we show the model results assuming an initial mass segregation of different slopes. We keep all the other parameters the same as before, i.e., $M_{\rm min} = 10^{5.5} M_\odot$, and $M_{\rm max} = 10^8 M_\odot$ for the ICMF and draw 300 GCs. To obtain an initial segregation, instead of drawing all the GCs from a single Hernquist profile, we split them into three mass bins of 100 GCs each. We draw the distances of the GCs in each group with a different Hernquist profile. For the low-mass GCs, we adopt a scale radius of $r_{0,\rm low} = 4.8$ kpc. To get different initial mass-segregation levels, we adopt $r_{0,\rm mid} = 2.8$ and 3.5 kpc for the intermediate-mass GCs, for the experiments shown in Figures 14 and 15, respectively; and, similarly, $r_{0,\rm high} = 0.4$ and 1.5 kpc, respectively. We also limit the initial radius range of the three groups by choosing different minimal radius $r_{\rm min}$ and maximal radius $r_{\rm max}$—for low-mass GCs, we set $r_{\rm min,low} =$ 1 kpc, and $r_{\rm max,low} = 5$ kpc; for intermediate-mass GCs, we set $r_{\rm min,low} = 0.5$ kpc, and $r_{\rm max,low} = 4$ kpc; and for high-mass GCs, we use $r_{\rm min,low} = 0.1$ kpc, and $r_{\rm max,low} = 2$ kpc. The slope of the initial mass segregation is -0.52 in Figure 14, and is -0.35 in Figure 15, comparable to and much smaller than the observed slope of -0.57, respectively. Then, we evolve them in an NFW halo of $10^{9.8} M_\odot$ and $c = 15$, which will not produce significant mass segregation with our fiducial setup. Not surprisingly, in such a relatively massive, normal-concentration halo, an initial mass segregation that is marginally weaker than the final one can basically reproduce the final mass segregation; whereas a significantly weaker initial mass segregation cannot.

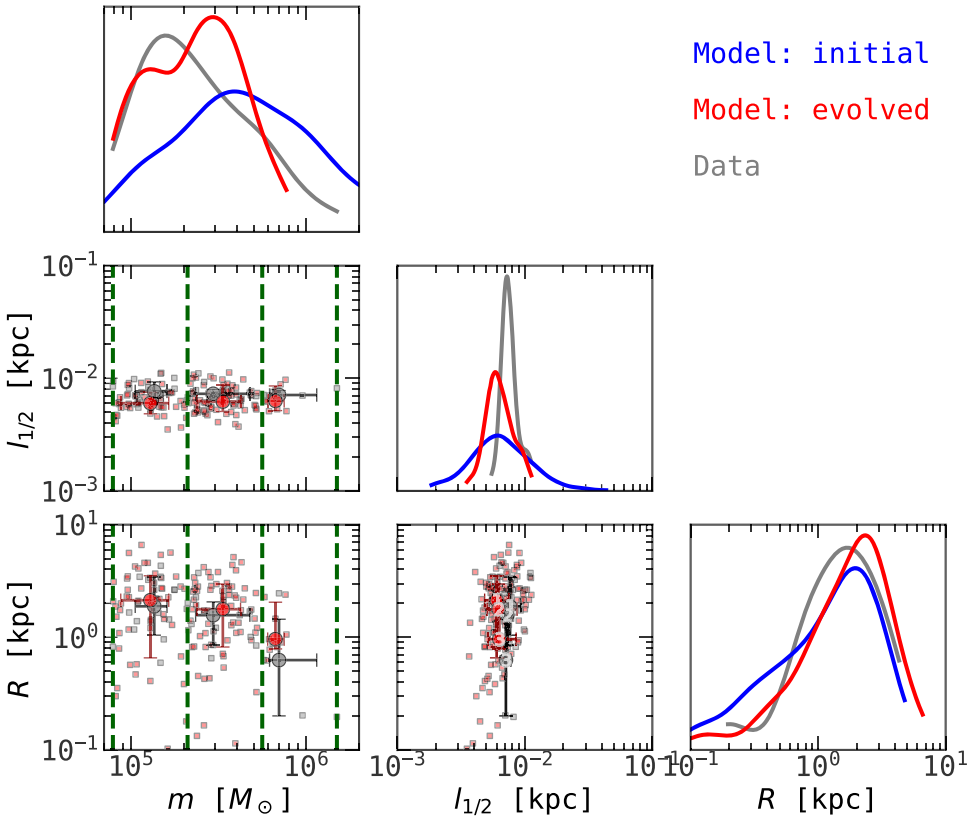

Figure 14. The same as Figures 5 and 7 but with a high-mass NFW host halo ($M_{\rm h} = 10^{9.8} M_\odot$, $c = 15$). 300 GCs are initialized in three mass groups with equal number, according to different Hernquist profiles such that the initial slope is -0.52.

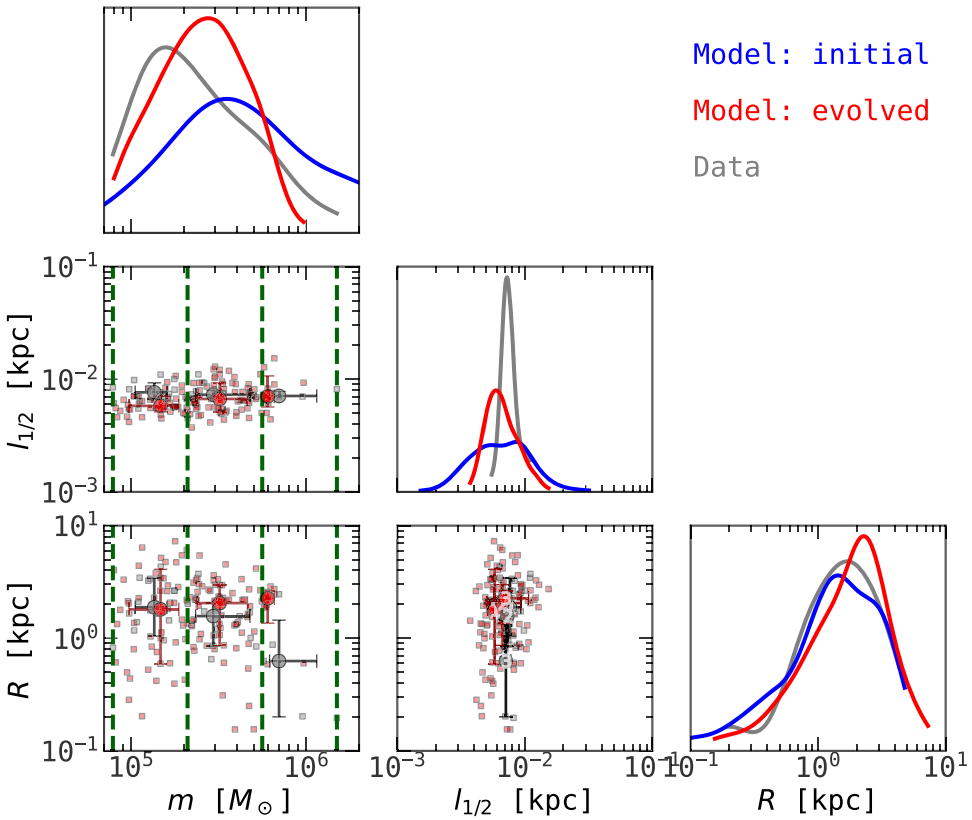

Figure 15. The same as Figure 14, but with a shallower initial mass-segregation slope of −0.35.

ORCID iDs

Jinning Liang https://orcid.org/0000-0001-8405-2921
Fangzhou Jiang https://orcid.org/0000-0001-6115-0633
Shany Danieli https://orcid.org/0000-0002-1841-2252
Andrew Benson https://orcid.org/0000-0001-5501-6008
Phil Hopkins https://orcid.org/0000-0003-3729-1684

References

Alexander, P. E. R., & Gieles, M. 2013, MNRAS Lett., 432, L1
Amorisco, N. C., & Loeb, A. 2016, MNRAS Lett., 459, L51
Banik, U., & van den Bosch, F. C. 2022, ApJ, 926, 215
Bar, N., Danieli, S., & Blum, K. 2022, ApJL, 932, L10
Behroozi, P. S., Wechsler, R. H., & Conroy, C. 2013, ApJ, 770, 57
Benavides, J. A., Sales, L. V., Abadi, M. G., et al. 2023, MNRAS, 522, 1033
Benson, A. J. 2020, MNRAS, 493, 1268
Benson, A. J., & Du, X. 2022, MNRAS, 517, 1398
Binney, J., & Tremaine, S. 2008, Galactic Dynamics (2nd ed.; Princeton, NJ: Princeton Univ. Press)
Boylan-Kolchin, M., Ma, C., & Quataert, E. 2008, MNRAS, 383, 93
Brown, G., & Gnedin, O. Y. 2021, MNRAS, 508, 5935
Burkert, A. 1995, ApJL, 447, L25
Burkert, A., & Forbes, D. A. 2020, AJ, 159, 56
Carleton, T., Errani, R., Cooper, M., et al. 2019, MNRAS, 485, 382
Chan, T. K. 2019, PhD thesis, Univ. of California, San Diego
Chandrasekhar, S. 1943, ApJ, 97, 255
Danieli, S., Dokkum, P. v., Conroy, C., Abraham, R., & Romanowsky, A. J. 2019, ApJL, 874, L12
Danieli, S., Greene, J. E., Carlsten, S., et al. 2023, ApJ, 956, 6
Danieli, S., van Dokkum, P., Trujillo-Gomez, S., et al. 2022, ApJL, 927, L28
Di Cintio, A., Brook, C. B., Dutton, A. A., et al. 2017, MNRAS Lett., 466, L1
Diemer, B., & Kravtsov, A. V. 2015, ApJ, 799, 108
Dutta Chowdhury, D., Bosch, F. C. V. d., & Dokkum, P. V. 2019, ApJ, 877, 133
Dutta Chowdhury, D., van den Bosch, F. C., & van Dokkum, P. 2020, ApJ, 903, 149
Dutton, A. A., & Macciò, A. V. 2014, MNRAS, 441, 3359
Elson, R. A. W., Fall, S. M., & Freeman, K. C. 1987, ApJ, 323, 54
Forbes, D. A., Alabi, A., Romanowsky, A. J., Brodie, J. P., & Arimoto, N. 2020, MNRAS, 492, 4874
Forbes, D. A., Gannon, J., Couch, W. J., et al. 2019, A&A, 626, A66
Forbes, D. A., Gannon, J. S., Romanowsky, A. J., et al. 2021, MNRAS, 500, 1279
Forbes, D. A., Read, J. I., Gieles, M., & Collins, M. L. M. 2018, MNRAS, 481, 5592
Foreman-Mackey, D., Hogg, D. W., Lang, D., & Goodman, J. 2013, PASP, 125, 306
Freundlich, J., Dekel, A., Jiang, F., et al. 2020, MNRAS, 491, 4523
Gan, J., Kang, X., van den Bosch, F. C., & Hou, J. 2010, MNRAS, 408, 2201
Gieles, M., Heggie, D. C., & Zhao, H. 2011, MNRAS, 413, 2509
Gieles, M., & Renaud, F. 2016, MNRAS Lett., 463, L103
Goerdt, T., Moore, B., Read, J. I., Stadel, J., & Zemp, M. 2006, MNRAS, 368, 1073
Greco, J. P., Greene, J. E., Strauss, M. A., et al. 2018, ApJ, 857, 104
Green, S. B., van den Bosch, F. C., & Jiang, F. 2021, MNRAS, 503, 4075
Guo, Q., Hu, H., Zheng, Z., et al. 2020, NatAs, 4, 246
Harris, W. E., Blakeslee, J. P., & Harris, G. L. H. 2017, ApJ, 836, 67
Harris, W. E., Harris, G. L., & Hudson, M. J. 2015, ApJ, 806, 36
Hénon, M. 1965, AnAp, 28, 992
Hernquist, L. 1990, ApJ, 356, 359
Hudson, M. J., Harris, G. L., & Harris, W. E. 2014, ApJL, 787, L5
Inoue, S. 2009, MNRAS, 397, 709
Iodice, E., Cantiello, M., Hilker, M., et al. 2020, A&A, 642, A48
Jiang, F., Dekel, A., Freundlich, J., et al. 2019, MNRAS, 487, 5272
Jiang, F., Dekel, A., Freundlich, J., et al. 2021, MNRAS, 502, 621
Jiang, F., & van den Bosch, F. C. 2017, MNRAS, 472, 657
Just, A., Khan, F. M., Berczik, P., Ernst, A., & Spurzem, R. 2011, MNRAS, 411, 653
Kaur, K., & Sridhar, S. 2018, ApJ, 868, 134
King, I. 1962, AJ, 67, 471
Lamers, H. J. G. L. M., Baumgardt, H., & Gieles, M. 2010, MNRAS, 409, 305
Liao, S., Gao, L., Frenk, C. S., et al. 2019, MNRAS, 490, 5182
Lim, S., Peng, E. W., Côté, P., et al. 2018, ApJ, 862, 82
Marleau, F. R., Habas, R., Poulain, M., et al. 2021, A&A, 654, A105
Modak, S., Danieli, S., & Greene, J. E. 2023, ApJ, 950, 178

Moreno, J., Danieli, S., Bullock, J. S., et al. 2022, NatAs, 6, 496
Müller, O., Marleau, F. R., Duc, P.-A., et al. 2020, A&A, 640, A106
Navarro, J. F., Frenk, C. S., & White, S. D. M. 1997, ApJ, 490, 493
Peñarrubia, J., Benson, A. J., Walker, M. G., et al. 2010, MNRAS, 406, 1290
Petts, J. A., Gualandris, A., & Read, J. I. 2015, MNRAS, 454, 3778
Quinlan, G. D. 1996, NewA, 1, 255
Read, J. I., Goerdt, T., Moore, B., et al. 2006, MNRAS, 373, 1451
Rong, Y., Guo, Q., Gao, L., et al. 2017, MNRAS, 470, 4231
Ryon, J. E., Bastian, N., Adamo, A., et al. 2015, MNRAS, 452, 525
Sales, L. V., Navarro, J. F., Peñafiel, L., et al. 2020, MNRAS, 494, 1848
Sánchez-Janssen, R., Côté, P., Ferrarese, L., et al. 2019, ApJ, 878, 18
Silk, J. 2017, ApJL, 839, L13
Spitler, L. R., & Forbes, D. A. 2009, MNRAS Lett., 392, L1
Spitzer, L. 1987, Dynamical Evolution of Globular Clusters (Princeton, NJ: Princeton Univ. Press)
Tremmel, M., Wright, A. C., Brooks, A. M., et al. 2020, MNRAS, 497, 2786
Trujillo-Gomez, S., Reina-Campos, M., & Kruijssen, J. M. D. 2019, MNRAS, 488, 3972
van den Bosch, F. C., Lewis, G. F., Lake, G., & Stadel, J. 1999, ApJ, 515, 50
van Dokkum, P., Abraham, R., Brodie, J., et al. 2016, ApJL, 828, L6
van Dokkum, P., Abraham, R., Romanowsky, A. J., et al. 2017, ApJL, 844, L11
van Dokkum, P., Danieli, S., Abraham, R., Conroy, C., & Romanowsky, A. J. 2019, ApJL, 874, L5
van Dokkum, P., Danieli, S., Cohen, Y., et al. 2018, Natur, 555, 629
van Dokkum, P., Shen, Z., Keim, M. A., et al. 2022, Natur, 605, 435
Wechsler, R. H., Bullock, J. S., Primack, J. R., Kravtsov, A. V., & Dekel, A. 2002, ApJ, 568, 52
Zentner, A. R., & Bullock, J. S. 2003, ApJ, 598, 49